Master Thesis

Studies of Solar Filament Formation and Eruption by Magnetohydrodynamic Simulations

Takafumi Kaneko

Space and Planetary Science Group

Department of Earth and Planetary Science

Graduate School of Science, The University of Tokyo

January, 23, 2014

要旨

太陽フィラメントの形成、放出メカニズムについて 2 次元磁気流体シミュレーションによる研究を行った。太陽フィラメントは高温のコロナ中に存在する低温高密度プラズマ雲であり、高密度プラズマはコロナ磁場によって支えられていると考えられている。フィラメントの低温高密度プラズマの生成機構は未だ謎であり、高密度プラズマを支える具体的な磁場構造についても不明な点が多い。また、フィラメントは突発的に宇宙空間へ放出され、フレアやコロナ質量放出を引き起こす原因となる。従って、太陽表面における磁気エネルギー開放現象を理解する上で重要な研究対象となっており、これまで様々な放出モデルが提示されて来たが、未だ完全な理解には至っていない。本修士論文では、まず、コロナアーケード磁場と浮上磁場の相互作用による放出現象について、その発生条件をパラメーター解析によって調べた。解析したパラメーターは実際に観測可能であるアーケード磁場のシア角、浮上磁場の磁場強度および出現位置である。結果として、浮上磁場の出現位置によって 2 つの異なる放出メカニズムが存在することが分かった。一方は浮上磁場とアーケード磁場のリコネクションによるメカニズムであり、もう一方は浮上磁場により圧縮されたアーケード磁場内で発生するリコネクションによるメカニズムである。前者は浮上磁場がアーケード磁場の磁気中性線近傍に出現した場合のメカニズムであり、放出は浮上磁場の磁場強度が小さいほど起こりやすい。後者は浮上磁場がアーケード磁場の端に出現した場合の放出メカニズムであり、放出は浮上磁場の磁場強度が大きいほど、また、出現位置がアーケード磁場に近いほど起こりやすい。後者に対する放出条件は、解析した 3 つのパラメーターについて簡単な式で表すことができ、放出現象を事前に予測する手がかりとなる可能性がある。

次に、Kuperus-Raadu モデルに代表される逆極性フィラメントの形成メカニズムについて、熱伝導、放射及び重力を考慮した 2 次元磁気流体シミュレーションを用いて研究した。新たなフィラメント形成モデルとしてレヴィテーション – コンデンセーションモデルを考案し、シミュレーションによって実証した。これは、コロナ下部の比較的密度の高いプラズマを磁束管の形成に伴ってコロナ上部へ持ち上げ (レヴィテーション)、熱不安定により低温高密度化させる (コンデンセーション) モデルである。二通りの加熱項と二通りの磁束管形成メカニズムをそれぞれ試した結果、すべての場合で磁束管内に熱不安定による低温高密度プラズマが生成され、逆極性フィラメントが形成された。加熱項の違いは熱不安定が励起されるまでの時間のみに影響することが分かった。さらに、このモデルが実際のフィラメントの密度 (周囲のコロナの 10−100 倍程度) を再現できることも確認した。

Abstract

We investigate the mechanisms for formation and eruption of filaments by two-dimensional MHD simulations. At first, we investigate the triggering mechanisms for the eruptions associated with the interaction between the newly emerging flux and the coronal arcade fields by two-dimensional MHD simulations including gravity. We perform parameter surveys with respect to arcade field height, magnetic field strength, and emerging flux location. Our results show that two possible mechanisms exist, which mechanism is dominant depends mostly on emerging flux location. One mechanism appears when the location of emerging flux is close to the polarity inversion line (PIL) of an arcade field. This mechanism requires reconnection between the emerging flux and the arcade field, as pointed out by the results of previous observational studies. The other mechanism appears when the location of emerging flux surrounds the edge of an arcade field. This mechanism does not require reconnection between the emerging flux and the arcade field but does demand reconnection in the arcade field above the PIL. Furthermore, we found that the eruptive condition for this mechanism can be represented by a simple formula. Our results also suggest the possibility of predicting whether or not an eruption will occur by investigating the amount of the emerging flux and the distribution of the ambient magnetic field.

Next, we investigate the formation mechanism of filaments which have the inverse polarity suggested by the Kuperus-Raadu model (the KR model). We propose a new mechanism named levitation-condensation model and demonstrated it by two-dimensional MHD simulations including thermal conduction, radiative cooling and gravity. In this model, the relatively dense plasma levitated by the flux rope triggers the thermal instability in the corona, leading to the formation of cool dense plasmas of the filaments. We tested two types of background heating and two types of formation mechanisms of the flux rope, and succeeded in reproducing the filament of the KR model in all the cases. We found that the type of heating only affects the process before the thermal instability. We also shows that our model has a possibility to reproduce the density of the filament, which is 10 - 100 times larger than that of surrounding corona, qualitatively.

Contents

1 General Introduction **3**

2 Filament Eruption by Newly Emerging Flux **8**

2.1 Introduction 8

2.2 SIMULATION MODEL 11

2.2.1 Basic Equations 11

2.2.2 Initial Conditions 12

2.3 RESULTS 15

2.3.1 Two mechanisms for formation and eruption of plasmoids . . . 15

2.3.2 Parameter Survey 16

2.3.3 Ejection Speed of Plasmoids 17

2.4 DISCUSSION 18

2.4.1 Conditions for CA-Type Eruptions 18

2.4.2 Conditions for RC-Type Eruptions 25

2.4.3 Formed Case 27

2.4.4 Comparison with Observations 28

2.5 SUMMARY 29

3 Filament Formation by Thermal Instability **40**

3.1 Introduction 40
3.2 Levitation-condensation model 42
3.3 Numerical settings 43
3.3.1 Basic equations and numerical scheme 43
3.3.2 Initial condition and boundary condition 46
3.3.3 Numerical scheme and grid size 49
3.3.4 Cases under investigations 52
3.4 RESULTS 54
3.5 DISCUSSION 66
3.5.1 Process for Triggering Thermal Instability 66
3.5.2 Temperature and Density of Condensation 71
3.5.3 Limitation of 2.5-dimensional simulations and prospect of three-dimensional simulations 73
3.6 SUMMARY 75

4 Conclusion **76**

Chapter 1

General Introduction

In this thesis, we investigate the mechanisms for formation and eruption of solar filaments. The solar filaments are cool dense plasma clouds in the corona (temperature: $4300 - 10000$ K, density: $10^9 - 10^{11}$ cm^{-3}). Typically, the filaments' plasma is 100 times cooler and denser than its surrounding corona (Labrosse et al., 2010). The filaments' plasmas are sustained by the coronal magnetic fields. Filaments appear in both the active regions ('active region filaments') and the quiet regions on the sun ('quiescent filaments'). Fig.1.1 shows the full disk Hα image of the sun by Big Bear Solar Observatory (BBSO). Filaments are observed as dark elongate structures against the disk of sun. The white regions on the surface correspond to the active regions and the other region is the quiet region. In Fig.1.1, active region filaments and quiescent filaments are observed simultaneously. Quiescent filaments tend to be several hundred Mm in length, approximately 100 Mm in height, their lifetime is several months, and the typical magnetic field strength is $3 - 15$ G, while active region filaments are of order 10 Mm in length, less than 10 Mm in height, their lifetime is minutes to hours and the typical field strength is $30 - 45$ G (Mackay et al., 2010). Filaments above the limb are observed as bright features and called

'prominences'. Quiescent prominences are located in the cavities which are darer than the surrounding corona in X-ray or EUV emissions due to low density (e.g. Berger et al., 2012).

Filaments are always located above the polarity inversion lines (PILs), across which signs of radial components of magnetic fields are reversed (Fig.1.2). There are two typical models for the magnetic structure, in which filaments' cool dense plasmas are located above the 'dips', the concave-up structure of magnetic field. One is the Kippenhahn-Schlüter model (Kippenhahn & Schlüter, 1957) in which the basic magnetic structure is the arcade field and the dip structure is formed by the weight of condensations (hereafter, the KS model). The other is the Kuperus-Raadu model (Kuperus & Raadu, 1974) in which the dip is a part of a twisted loop-like magnetic structure (hereafter, the KR model). The observational difference between these two models is the magnetic polarity inside the filament relative to the ambient overlying magnetic arcade (Fig.1.3). The KS model has normal polarity, while the KR model has inverse polarity. The statistical study shows that both normal and inverse polarity filaments are existing in the solar atmosphere (Leroy et al., 1984).

Some of filaments suddenly erupt, and evolve to coronal mass ejections (CMEs). Many models about the filament eruptions and CMEs has been proposed. The interaction between the pre-existing arcade field and the newly emerging flux is one of these models (Feynman & Martin, 1995; Chen & Shibata, 2000; Notoya, 2006). In chapter 2, the mechanism of eruption associated with the emerging flux and the parameter dependence of the eruptive conditions are investigated.

The formation mechanism of the filaments' cool dense plasmas is also still under debate. One model to explain it is the evaporation-condensation model (Antiochos & Klimchuk, 1991), which is based on the theory of the thermal instability (Field,

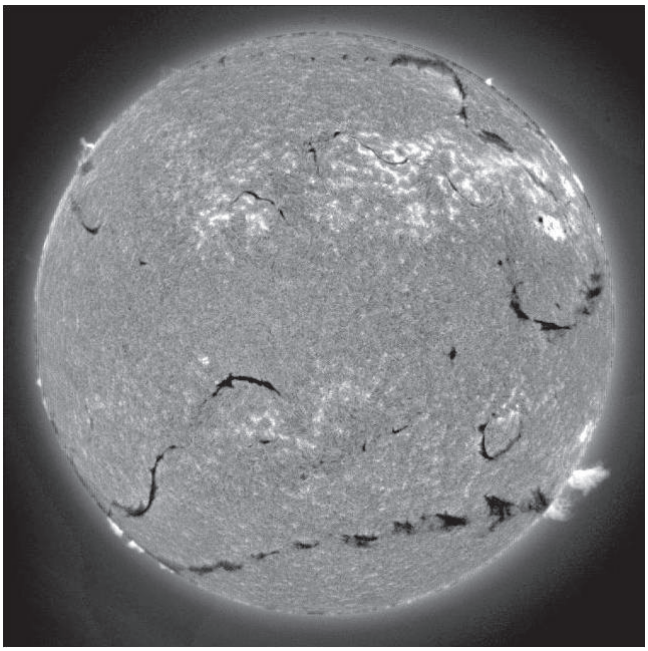

Figure 1.1: Hα image by Big Bear Solar Observatory.

1965) and the thermal stability of coronal loops (Rosner et al., 1978). Xia et al. (2012) succeeded in reproducing the KS type filament (prominence) with this formation model by two-dimensional self-consistent MHD simulations including radiative cooling, thermal conduction and gravity (Fig.1.4). On the other hand, the model to reproduce the filament of the KR model has not established yet. In chapter 3, a new idea to reproduce the filament of the KR model is proposed and demonstrated by two-dimensional self-consistent MHD simulations.

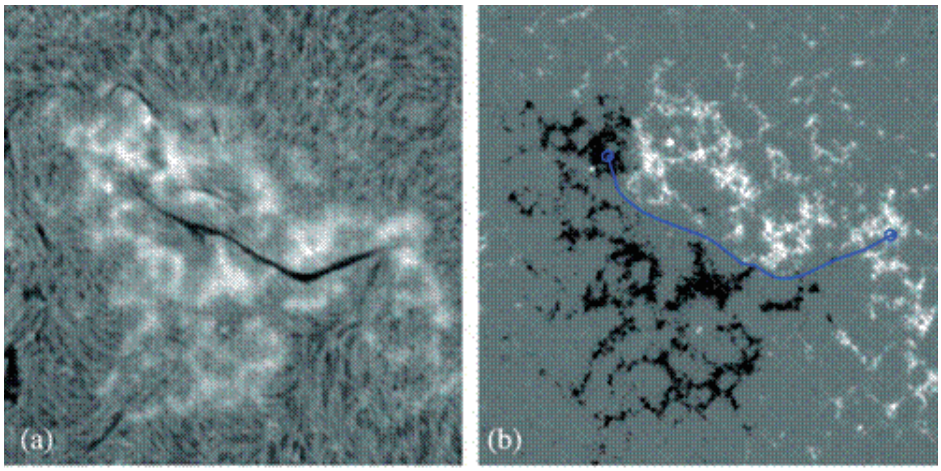

Figure 1.2: Active regions NOAA 9997 and NOAA 10000 on 2002 June 18 at 15:47 UT: (a)Hα image from BBSO (b)MDI magnetogram with path of filament (blue line); White represents positive polarity and black represents negative polarity (Bobra et al., 2008).

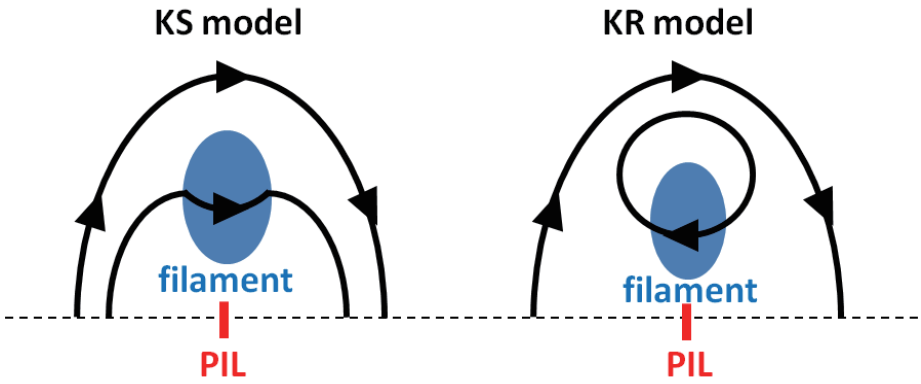

Figure 1.3: Schematic drawings of the Kippenhahn-Schlüter model and the Kuperus-Raadu model.

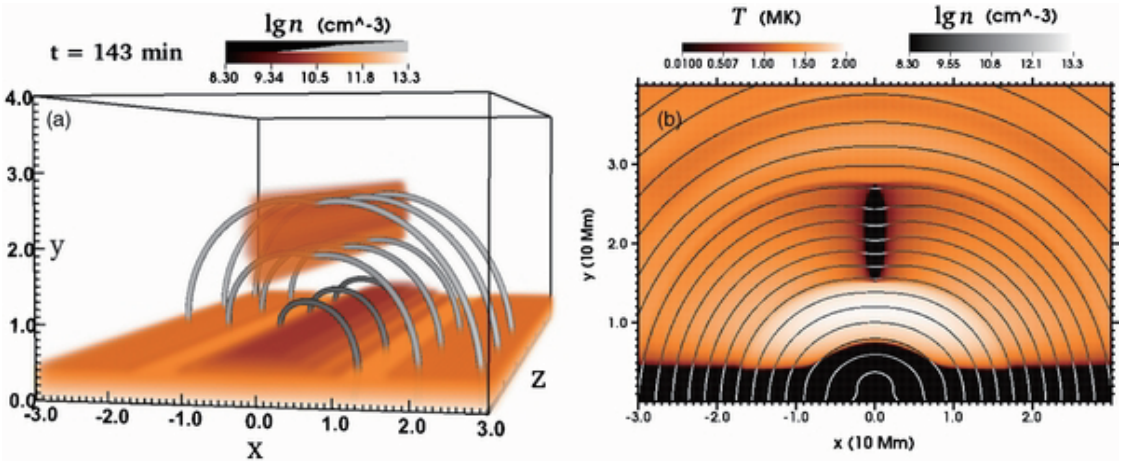

Figure 1.4: Kippenhahn-Schlüter prominence in Xia et al. (2012). (a)3D impression of the prominence shown by the number density and selected magnetic field lines. The bar above the color bar shows the opacity of corresponding colors. (b)The temperature and the projected field lines colored according to the local density.

Chapter 2

Filament Eruption by Newly Emerging Flux

2.1 Introduction

Many kinds of eruptive phenomena, such as flares, filament eruptions and coronal mass ejections (CMEs), can be seen in the solar atmosphere. A large-scale quiescent filament, whose length can reach several hundred Mm, remains for a few days or months in the corona before suddenly erupting, while a filament in an active region, whose spatial size is less than 10 Mm, usually has a shorter lifetime than that of the associated active region (Labrosse et al., 2010; Mackay et al., 2010). Eruptive flares and CMEs are so often observed with filament eruptions (Gopalswamy et al., 2003; Jing et al., 2004; Liu et al., 2012) that it is widely believed that these eruptive phenomena are triggered by the same global magnetohydrodynamic (MHD) process by which free magnetic energy stored in the coronal magnetic field is released as a form of thermal and/or kinematic energy.

Many models and theories about the triggers have been created from both ob-

servational and theoretical studies (Chen, 2011), however, the exact mechanism by which they occur happens is still unclear. The interaction between newly emerging flux and coronal magnetic fields is one candidate. Many observational studies report that newly emerging flux exists near the filament channel just before the occurrence of a filament eruption (e.g. Feynman & Martin, 1995; Wang & Sheeley, 1999; Xu et al., 2008; Pevtsov et al., 2012). Feynman & Martin (1995) found in a statistical study that quiescent filament eruptions tended to occur when the polarity of newly emerging flux and the magnetic field of a filament channel were favorable for reconnection. The observational statistical study of Xu et al. (2008) confirmed the results of Feynman & Martin (1995) and found that the location of emerging flux relative to the filament channel heavily affected the occurrence of eruptions.

Chen & Shibata (2000) performed a theoretical study by using two-dimensional MHD simulations. They used the quadrupole magnetic structure, which consisted of a detached flux rope and an overlying magnetic loop as an initial condition, and were able to create emerging flux by changing the magnetic field at the bottom boundary. As a result, the system entered a non-equilibrium state and the flux rope was driven upward by the reconnection beneath it. Kusano et al. (2012), through the use of three-dimensional zero-β MHD simulations, showed that emerging flux introduced into the PIL can destabilize sheared magnetic arcade fields in the corona and cause plasma eruptions . Note that they regarded emerging flux as no more than a means of changing the magnetic field distribution at the bottom boundary of the arcade field.

Notoya (2006) demonstrated a theoretical model of a filament eruption associated with emerging flux by using three-dimensional MHD simulations, which included gravity. A flux tube buried in the convection zone entered the corona by

magnetic buoyancy in a self-consistent manner. The emerging flux deformed the arcade field, which caused reconnection, and resulted in the formation and eruption of a filamentary structure. One of the differences between Kusano et al. (2012) and Notoya (2006) was the location of emerging flux; it was on the PIL in the former, while it was apart from the PIL in the latter.

The length of the filamentary structure formed in the simulation of Notoya (2006) has, at most, the same spatial scale of the emerging flux region. This is much smaller than those of the observed large-scale quiescent filaments. Moreover, the filamentary structure in the simulations erupts immediately after forming, in contrast to the long lifetime of the quiescent filaments. These small-scale and quickly erupting filaments have been observed before (Wang et al., 2000; Sakajiri et al., 2004; Ren et al., 2008), and are called 'miniature filaments'. It has been found that miniature filaments and quiescent filaments share several common features. For example, a two-ribbon flare is often observed after an eruption. In addition, most miniature filament eruptions occur in a cancellation region or a newly emerging flux region, so reconnection is therefore thought to play an important role. Wang et al. (2000) concluded that miniature filament eruptions are the 'analogues' of quiescent-filament eruptions, and that the triggering mechanisms of these plasma eruptions may be the same.

In this chapter we aim to determine the conditions under which eruptions occur due to the interaction between newly emerging flux and coronal arcade fields and express them as a formula by using observable variables.

We perform MHD simulations, based on a model similar to that of Notoya (2006). The parameters for our survey are arcade field height, magnetic field strength, and emerging flux location.

2.2 SIMULATION MODEL

2.2.1 Basic Equations

We solve nonlinear, time-dependent, resistive, compressible MHD equations in a rectangular computational box. The simulations are 2.5-dimensional, i.e., all three components in velocity and magnetic fields are taken into account in a two-dimensional x, y-domain. The gas is assumed to be ideal with the ratio of specific heats $\gamma = 5/3$. Thermal conduction, radiative cooling and viscosity are absent in our simulations. The equations are

$$\frac{\partial \rho}{\partial t} + \nabla \cdot (\rho \boldsymbol{v}) = 0, \tag{2.1}$$

$$\frac{\partial (\rho \boldsymbol{v})}{\partial t} + \nabla \cdot \left(\rho \boldsymbol{v}\boldsymbol{v} + p\boldsymbol{I} - \frac{\boldsymbol{B}\boldsymbol{B}}{4\pi} + \frac{B^2}{8\pi}\boldsymbol{I} \right) - \rho \boldsymbol{g} = 0, \tag{2.2}$$

$$\frac{\partial}{\partial t}\left(\frac{p}{\gamma - 1} + \frac{1}{2}\rho \boldsymbol{v}^2 + \frac{B^2}{8\pi} \right) + \nabla \cdot \left[\left(\frac{\gamma}{\gamma - 1} p + \frac{1}{2}\rho \boldsymbol{v}^2 \right) \boldsymbol{v} + \frac{c}{4\pi} \boldsymbol{E} \times \boldsymbol{B} \right] - \rho \boldsymbol{g} \cdot \boldsymbol{v} = 0, \tag{2.3}$$

$$\frac{\partial \boldsymbol{B}}{\partial t} = -c \nabla \times \boldsymbol{E}, \tag{2.4}$$

$$\boldsymbol{E} = -\frac{1}{c} \boldsymbol{v} \times \boldsymbol{B} + \frac{4\pi\eta}{c^2} \boldsymbol{J}, \tag{2.5}$$

$$\boldsymbol{J} = \frac{c}{4\pi} \nabla \times \boldsymbol{B}, \tag{2.6}$$

where η is the magnetic diffusion rate, $\boldsymbol{g} = (0, -g_{\rm pho})$ is the gravitational acceleration, and $g_{\rm pho} > 0$ is constant. Temperature is derived from the equation of state:

$$T = \frac{m}{k_B} \frac{p}{\rho}, \tag{2.7}$$

where m is the mean molecular mass (assumed constant), and k_B is the Boltzmann's constant. The normalized units of length, velocity, and density are $H_{\rm pho} = 310$km,

$C_{s,\mathrm{pho}} = 12\mathrm{km/s}$, and $\gamma\rho_{\mathrm{pho}} = 2.8 \times 10^{-7}\mathrm{g/cm^3}$, respectively, where the subscript 'pho' means the typical value in the photosphere, and H_{pho} and $C_{s,\mathrm{pho}}$ are scale height and speed of sound, respectively. The other normalized units are combinations of these units: time is $H_{\mathrm{pho}}/C_{s,\mathrm{pho}} = 26\mathrm{s}$, temperature is $(m/k_B\gamma)C_{s,\mathrm{pho}}^2 = 10^4\mathrm{K}$, magnetic field is $(\rho_{\mathrm{pho}}/\gamma)^{1/2}C_{s,\mathrm{pho}} = 490\mathrm{G}$, and gravitational acceleration is $C_{s,\mathrm{pho}}^2/H_{\mathrm{pho}} = \gamma g_{\mathrm{pho}} = 4.5 \times 10^4\mathrm{cm \cdot s^{-2}}$.

We use anomalous resistivity (e.g Yokoyama & Shibata, 1994) to trigger a Petschek-type reconnection:

$$\eta = \begin{cases} 0 & (v_d \le v_c) \\ \eta_0 \left(v_d/v_c - 1\right)^2 & (v_d \ge v_c), \end{cases} \tag{2.8}$$

where $v_d = mJ/e\rho$ is drift velocity, e is elementary charge, and the normalized values of the parameters are $\eta_0 = 0.01$ and $v_c = 1000$. We restrict the value of η to $\eta_{\max} = 1.0$.

2.2.2 Initial Conditions

Fig.2.1 shows the initial vertical distribution of temperature, density, gas pressure, and magnetic pressure. The background gas consists of four layers:

$$T(y) = \begin{cases} T_{\mathrm{pho}} - \left(d\left|\dfrac{dT}{dy}\right|_{\mathrm{ad}}\right) y, & (y \le y_{\mathrm{pho}}) \quad (2.9) \\ T_{\mathrm{pho}}, & (y_{\mathrm{pho}} \le y \le y_{\mathrm{tr}}) \quad (2.10) \\ T_{\mathrm{pho}} + (T_{\mathrm{cor}} - T_{\mathrm{pho}})\dfrac{y - y_{\mathrm{tr}}}{y_{\mathrm{cor}} - y_{\mathrm{tr}}}, & (y_{\mathrm{tr}} \le y \le y_{\mathrm{cor}}) \quad (2.11) \\ T_{\mathrm{cor}}, & (y_{\mathrm{cor}} \le y) \quad (2.12) \end{cases}$$

where $T_{\mathrm{pho}} = 1$ (10^4K), $T_{\mathrm{cor}} = 100$ (10^6K), $y_{\mathrm{pho}} = 0$, $y_{\mathrm{tr}} = 10$ (3100km), and $y_{\mathrm{cor}} = 14$ (4340km). This modeling of the solar atmosphere represents the subphotospheric convective zone, the photosphere/chromosphere, the transition layer and the corona,

respectively. $|dT/dy|_{\rm ad} = (\gamma-1)/\gamma$ is the adiabatic gradient, and d is a dimensionless constant which determines the stability of convection. Because d is chosen to be 1.015, the convective zone is slightly unstable. The initial gas pressure is determined with the equation of gravitational stratification:

$$p(y) = p_{\rm pho} \exp\left[- \int_{y_{\rm pho}}^{y} \frac{m g_{\rm pho}}{k_B T(y')} dy' \right]. \tag{2.13}$$

We use a Gold-Hoyle type flux tube as a model of emerging flux (Magara, 2001, 2004). In $(x-x_e)^2 + (y-y_e)^2 \leq r_e^2$, magnetic field is given as

$$B_x = \frac{-B_e q (y-y_e)}{1+q^2\left([x-x_e]^2+[y-y_e]^2\right)}, \tag{2.14}$$

$$B_y = \frac{B_e q (x-x_e)}{1+q^2\left([x-x_e]^2+[y-y_e]^2\right)}, \tag{2.15}$$

$$B_z = \frac{B_e}{1+q^2\left([x-x_e]^2+[y-y_e]^2\right)}, \tag{2.16}$$

where the axis of the flux tube $y_e = -7$ (2170km), radius $r_e = 4$ (1240km), pitch number $q = 0.5$, and the length of the one helical turn along the axis is $2\pi/q = 4\pi$ (3896km). In our simulations, B_e takes the values of $11, 13, 15$ and 17 (5300G $-$ 8300G), and x_e is set in the range from -40 to 40. This flux tube model satisfies the force-free condition inside itself, so the initial gas pressure in the flux tube is

$$p_{\rm tube} = p(y) - \frac{B_e^2}{8\pi} \frac{1}{1+q^2 r_e^2} \tag{2.17}$$

for the pressure balance in a horizontal direction between the inside and the outside of the flux tube. The temperature of the flux tube is the same as its outside so that the density of the flux tube is lower than its outside, causing magnetic buoyancy.

The magnetic arcade field is described as

$$B_x = \left(\frac{2L}{\pi a}\right) B_a \sin\left(\frac{\pi}{2L}x\right) \exp\left[-\frac{y}{a}\right], \tag{2.18}$$

$$B_y = B_a \cos\left(\frac{\pi}{2L}x\right) \exp\left[-\frac{y}{a}\right], \tag{2.19}$$

$$B_z = -\sqrt{1-\left(\frac{2L}{\pi a}\right)^2} B_a \sin\left(\frac{\pi}{2L}x\right) \exp\left[-\frac{y}{a}\right], \tag{2.20}$$

where $B_a = 0.05$ (24G), $L = 40$ (1.2×10^4km), and a is set in the range from 50 to 100. L and a represent the half width and the magnetic scale height of the arcade field, respectively. We define the shear angle of the arcade field θ as

$$\theta = \tan^{-1}\left(-\frac{B_z}{B_x}\right) = \tan^{-1}\left(\sqrt{\left(\frac{\pi a}{2L}\right)^2 - 1}\right). \tag{2.21}$$

When L is constant, the larger a is, the larger θ is. Because the arcade field is also force-free, the initial condition is in a mechanical equilibrium.

As for the relative arrangement between the emerging flux and the arcade fields, we refer to the right arcade toward the flux tube in the initial condition as 'counter-arranged arcade' because the polarity arrangement is in reverse order, and the left arcade as 'co-arranged arcade' because the polarity arrangement is in the same order as emerging flux (Fig.2.2).

The horizontal grid width is uniform, with $\Delta x = 0.4$. The vertical grid width is not uniform, with $\Delta y = 0.4$ near the flux tube and $\Delta y = 4.0$ in the vicinity of the top boundary. The simulation box is $-120 < x < 120$ and $-20 < y < 1204$. The calculation scheme is a modified Lax-Wendroff method (Rubin & Burstein,1967) with artificial viscosity (Lapidus,1967). A periodic boundary condition is applied to the left and right boundaries, and a free boundary condition is applied to the top

and the bottom boundaries.

2.3 RESULTS

2.3.1 Two mechanisms for formation and eruption of plasmoids

Our simulations suggest two mechanisms for the formation and eruption of plasmoids: one is due to compression of the arcade field by the emerging flux (hereafter 'CA-type' mechanism), and the other is due to reconnection coupling as a consequence of multipoint reconnections between the arcade field and the emerging flux (hereafter 'RC-type' mechanism). In both mechanisms, the plasmoid is accelerated by reconnection outflow. In spite of the distinct mechanisms, both the CA-type and the RC-type eruptions succeed in constructing a cusp hot structure (Tsuneta et al., 1992) in the standard CSHKP model (Carmichael, 1964; Sturrock, 1966; Hirayama, 1974; Kopp & Pneuman, 1976).

Fig.2.3 shows a time evolution of the CA-type mechanism in the case of $(B_e, x_e, a) = (15, 0, 100)$. The flux tube initially buried in the convection zone expands rapidly after entering the corona ($t = 70$). The magnetic field strength of the arcade compressed by expanding emerging flux becomes larger ($t = 100$). As a result, reconnection occurs inside the neighboring arcades above each PIL around $x = \pm 40$, leading to the formation of plasmoids ($t = 130$). One of the plasmoids is accelerated upward by reconnection outflow ($t = 150$). The plasmoid originating from the counter-arranged arcade continues to rise up even after reconnection stops. However, the plasmoid originating from the co-arranged arcade is pulled by a downward magnetic tension force from the overlying arcade field, which is formed by the re-

connection between the arcade field and emerging flux.

Fig.2.4 shows a time evolution of the RC-type mechanism in the case of $(B_e, x_e, a) = (11, 40, 100)$. An eruption of this type occurs when the emerging flux appears close to the PIL of the counter-arranged arcade. In contrast to the CA-type, since the location x_e is close to the PIL, the emerging flux expands the arcade field rather than compressing it ($t = 90$). Due to the contact of the anti-directional field lines, a current sheet forms between the arcade and emerging flux. The reconnections are triggered at multiple points in this sheet almost simultaneously, and a plasmoid grows ($t = 150$). The hot outflow from a right-side reconnection point, which is slightly intense compared with that from the left-side reconnection point, passes through the boundary region between the arcade and the emerging flux, and links to the inflow region of the left-side reconnection point ($t = 172$). The left-side reconnection is promoted by the outflow from the right-side reconnection point and a plasmoid erupts ($t = 220$). Fig.2.5 is the extended view of the reconnection coupling. The outflow from one reconnection point at $(x, y) = (70, 55)$ reaches the other X-point at $(x, y) = (5, 60)$ and promotes the reconnection there, leading to the growth and eruption of a plasmoid. Reconnection points in the current sheet appear in random positions as a result of a resistive instability in which the seed perturbations are imposed by numerical noises.

2.3.2 Parameter Survey

The results of our parameter survey with respect to B_e and x_e are shown in Fig.2.6. The filled circles represent the cases in which a plasmoid forms and erupts (hereafter 'erupted case'), the triangles represent the cases in which plasmoid forms but does not erupt (hereafter 'formed case'), and the crosses represent the cases in which

no plasmoid forms (hereafter 'unformed case'). CA-type eruptions occur more frequently with higher values of emerging flux field strength, and at locations closer to the arcade field. However, when the location of the emerging flux is too close to the PIL, eruptions fail to occur. RC-type eruptions can be seen when the location of the emerging flux is just around the PIL. RC-type eruptions occur more frequently with smaller values of emerging flux field strength, and at locations closer to the PILs of counter-arranged arcade fields.

Fig.2.7 shows the results of the parameter survey with respect to the magnetic scale height a in each $(B_e, x_e) = (15, 0)$, $(17, 0)$, $(13, 40)$, and$(11, 40)$ case. When $a = 100$, the cases of $(B_e, x_e) = (17, 0)$ and $(15, 0)$ belong to the CA-type, and the cases of $(B_e, x_e) = (13, 40)$ and $(11, 40)$ belong to the RC-type. Fig.2.7 shows that eruptions are likely to occur when a is large.

2.3.3 Ejection Speed of Plasmoids

The mean ejection speed of each plasmoid is calculated from the time evolution of its height. Fig.2.8 (a) shows the time evolution of height, and Fig.2.8 (b) shows the mean ejection speed of the plasmoid in each eruptive case. When the field strength of the emerging flux is large, the mean ejection speed is high. The dependence on χ in the same field strength of the emerging flux is relatively small. This means that the kinetic energy of the plasmoid comes from the magnetic energy of the emerging flux, i.e., the magnetic energy of the emerging flux is stored as it is in the arcade field , and the reconnection releases the stored magnetic energy as kinetic energy of the plasmoid.

There are two cases in which plasmoids descend. This is caused by the downward magnetic tension force of the large overlying loop, which is formed by the

reconnection between the co-arranged arcade and the emerging flux in the CA-type mechanism.

2.4 DISCUSSION

In this section, we discuss the reasons why the results of the parameter survey show the tendencies in Figs.2.6 and 2.7 and attempt to outline the eruptive conditions of each mechanism.

2.4.1 Conditions for CA-Type Eruptions

When the flux tube emerges around the edge of the arcade field, the expanding emerging flux compresses the arcade field, which generates a current above the PIL. If the current exceeds a certain threshold, reconnection occurs, resulting in the formation and eruption of a plasmoid. Therefore, deriving the eruptive conditions requires the evaluation of the current density inside the compressed arcade field, the extent to which the emerging flux compresses the arcade field, and the threshold of the current to trigger the reconnection.

First, we evaluate the extent to which the emerging flux compresses the arcade field. This can be estimated by considering the balance of magnetic pressures between the arcade and emerging flux. Fig.2.9 (a) shows magnetic pressure (solid line), gas pressure (dashed line), and total pressure (dotted line). The region of the emerging flux is $x < 18$, the region of the arcade field is $x > 25$, and $18 < x < 25$ is a high-β region. The high-β region is composed of the material fallen from the top of the emerging flux where 'dense sheath' (Isobe et al., 2006) is formed. As shown in Fig.2.9 (a), the magnetic pressures of the emerging flux and the arcade field are

balanced with the gas pressure of the high-β region. Therefore, it is possible to regard the magnetic pressures of the emerging flux and the arcade field as being in balance with each other. Fig.2.9 (b) shows the x-directional forces of the magnetic pressure gradient, gas pressure gradient, and magnetic tension. We find that the magnetic tension force is negligible compared with the other two forces. These findings suggest that the magnetic pressures of the emerging flux and the arcade field are in balance. Next, we postulate the self-similar time evolution of the magnetic fields , assuming that the parameters of the arcade field (B_a, L, a) are changed into $(\bar{B_a}, fL, \bar{a})$ after being compressed. The extent that the emerging flux can compress the arcade is expressed by the compression rate of the arcade field f. From the conservation of magnetic flux,

$$\Phi_a = \int_0^L B_a \cos\left(\frac{\pi}{2L}x\right) \exp\left[-\frac{y}{a}\right] dx \quad = \quad \int_0^{fL} \bar{B_a} \cos\left(\frac{\pi}{2fL}x\right) \exp\left[-\frac{y}{\bar{a}}\right] dx,$$

which leads to

$$\Phi_a = \frac{2L}{\pi} B_a \exp[-\frac{y}{a}] = \frac{2fL}{\pi} \bar{B_a} \exp[-\frac{y}{\bar{a}}]. \tag{2.22}$$

The condition

$$\bar{B_a} = \frac{B_a}{f}, \quad \bar{a} = a \tag{2.23}$$

satisfies Eq.(2.22). Actually, $\bar{a} = a$ is just an assumption, but when y is small enough compared with a, the effect from a change in a is negligible, which is confirmed (not shown) in our results. For the emerging flux, (B_e, q, r_e) changed into $(\bar{B_e}, \bar{q}, \bar{r_e})$ after compression. The expanded emerging flux is described as

$$\bar{\boldsymbol{B}}_{\boldsymbol{e}} = \bar{B_\theta} \boldsymbol{e}_\theta + \bar{B_z} \boldsymbol{e}_z, \tag{2.24}$$

where

$$\bar{B}_\theta = \bar{q} r \bar{B}_z, \tag{2.25}$$

$$\bar{B}_z = \bar{B}_e F(r), \tag{2.26}$$

and where $\boldsymbol{e}_\theta$ and $\boldsymbol{e}_z$ are unit vectors of azimuthal direction and z-direction, respectively, and $F(r)$ is an arbitrary decreasing function of r which satisfies $F(0) = 1$. From the conservation of magnetic flux,

$$\Phi_e = \int_0^{r_e} \frac{B_e q r}{1 + q^2 r^2} dr = \int_0^{\bar{r_e}} \bar{B}_e \bar{q} r F(r) dr, \tag{2.27}$$

which leads to

$$\Phi_e = \frac{B_e}{2q} \ln(1 + q^2 r_e^2) = \bar{B}_e \bar{q} \bar{r_e}^2 G(\bar{r_e}), \tag{2.28}$$

where

$$G(\bar{r_e}) \equiv \frac{1}{\bar{r_e}^2} \int_0^{\bar{r_e}} r F(r) dr. \tag{2.29}$$

Because $F(r)$ is a monotonically decreasing function of r,

$$\frac{1}{2} F(\bar{r_e}) \leq G(\bar{r_e}). \tag{2.30}$$

The emerging flux can expand until its magnetic pressure is balanced with that of the arcade field:

$$\frac{(1 + \bar{q}^2 \bar{r_e}^2) \bar{B_e}^2 F(r)^2}{8\pi} = \frac{\bar{B_a}^2}{8\pi} \exp\left[-\frac{2y}{\bar{a}}\right]. \tag{2.31}$$

By substituting Eq.(2.22) and Eq.(2.28) into Eq.(2.31) and using the approximation that $\bar{q}\bar{r_e} \gg 1$,

$$\frac{\Phi_e}{\Phi_a} = \frac{\pi \bar{r_e}}{2fL} \frac{G(\bar{r_e})}{F(\bar{r_e})}. \tag{2.32}$$

From the positional relation between the emerging flux and the arcade field, for the counter-arranged arcade field, as $\chi L \equiv L - x_e$,

$$2L = x_e + \bar{r_e} + f(2L - x_e), \tag{2.33}$$

and for the co-arranged arcade field, as $\chi L \equiv x_e + L$,

$$-2L = x_e - \bar{r_e} - f(x_e + 2L), \tag{2.34}$$

which leads to

$$\bar{r_e} = (1 - f)(1 + \chi)L, \tag{2.35}$$

where χL represents the absolute distance between the PIL of the arcade field and the location of the emerging flux. By using Eqs.(2.30), (2.32), and (2.35),

$$\frac{\zeta}{1+\chi} > \frac{\pi}{4}\frac{1-f}{f}, \tag{2.36}$$

where $\zeta \equiv \Phi_e/\Phi_a$. From this formula, the extent of compression (in this case minimum value of f) can be estimated. By assuming that reconnection occurs when $f < f_{\rm cr}$, the necessary condition for triggering an eruption is

$$\frac{\zeta}{1+\chi} > \frac{\pi}{4}\frac{1-f_{\rm cr}}{f_{\rm cr}}. \tag{2.37}$$

If the force-free condition, $(\nabla \times \bar{\boldsymbol{B}}_{\boldsymbol{e}}) \times \bar{\boldsymbol{B}}_{\boldsymbol{e}} = 0$, is satisfied, the function $F(r)$ is derived to be the Gold-Hoyle type geometry:

$$\frac{d}{dr}\left\{\left(1 + q^2 r^2\right) F(r)\right\} = 0, \tag{2.38}$$

from which we obtain

$$F(r) = \frac{1}{1+q^2r^2}. \tag{2.39}$$

When a static state is realized due to the balance of magnetic pressures, the emerging flux can be assumed to be under a force-free condition. In this case, the eruptive conditions are easily derived by using Eq.(2.32), Eq.(2.35) and the approximation of $\bar{q}\bar{r_e} \gg 1$:

$$\frac{\zeta}{1+\chi} > \kappa \frac{1-f_{\rm cr}}{f_{\rm cr}}, \tag{2.40}$$

where

$$\kappa = \frac{\pi}{4}\ln(\bar{q}^2\bar{r_e}^2). \tag{2.41}$$

Because of the logarithmic dependence, the value of κ can be regarded as constant even when the value of $\bar{r_e}$ varies. The value of κ is 3.6 to 5.3 when $\bar{r_e}$ is 20 to 60 in our simulations.

Next, we discuss $f_{\rm cr}$. We use anomalous resistivity, which depends on the drift velocity $v_d = mJ/e\rho$ (see Eq.(2.8)). The current density inside the arcade field in the initial state J is

$$J = \sqrt{\left(\frac{\pi}{2L}\right)^2 - \left(\frac{1}{a}\right)^2} B_a \exp\left[-\frac{y}{a}\right] = \frac{\pi}{2L}\sin\theta B_a \exp\left[-\frac{y}{a}\right]. \tag{2.42}$$

The current density inside the compressed arcade $\bar{J}$ is

$$\bar{J} = \frac{\pi}{2fL}\sin\bar{\theta}\bar{B_a}\exp\left[-\frac{y}{\bar{a}}\right] = \frac{J}{f^2}, \tag{2.43}$$

where Eq.(2.23) and the approximation of

$$\frac{\sin\bar{\theta}}{\sin\theta} = \sqrt{\frac{(\pi a)^2 - (2fL)^2}{(\pi a)^2 - (2L)^2}} \approx 1 \tag{2.44}$$

are used. The drift velocity $\bar{v_d}$ inside the compressed arcade is

$$\bar{v_d} = \frac{m\bar{J}}{e\bar{\rho}} = \frac{v_d}{f}, \tag{2.45}$$

where the density inside the compressed arcade is assumed to be $\bar{\rho} = \rho/f$. Assuming that reconnection occurs when drift velocity exceeds a certain critical value, namely $\bar{v_d} > v_{\rm cr}$, then

$$f < \frac{v_d}{v_{\rm cr}} = f_{\rm cr} \tag{2.46}$$

is the condition for f to trigger the reconnection. By combining Eq.(2.40) and Eq.(2.46), the eruptive condition is

$$\frac{\zeta}{1+\chi} > \kappa', \tag{2.47}$$

where

$$\kappa' = \kappa\frac{v_{\rm cr} - v_d}{v_d}. \tag{2.48}$$

The theory of resistivity in the corona is still unclear, so the dependence on v_d and other parameters might be more complex. This model of κ' is available for a qualitative explanation for our simulation results.

The obtained model can be compared with our simulation results. For this purpose, ζ, Φ_e, and Φ_a are measured from the simulations. Fig.2.10 shows the amount of the magnetic flux introduced into the photosphere and the corona. The

dashed line in Fig.2.10 is the initial magnetic flux of the emerging flux computed by the middle term of Eq.(2.28). The amount of magnetic flux introduced into the photosphere and the corona is defined as follows:

$$\Phi_{\rm pho}(t) = \frac{1}{2}\left(\Phi(y_{\rm pho},t) - \Phi_{\rm ar}(y_{\rm pho})\right), \tag{2.49}$$

$$\Phi_{\rm cor}(t) = \frac{1}{2}\left(\Phi(y_{\rm cor},t) - \Phi_{\rm ar}(y_{\rm cor})\right), \tag{2.50}$$

$$\tag{2.51}$$

where

$$\Phi(y,t) = \int_{x_{\rm min}}^{x_{\rm max}} |B_y(x,y,t)|dx, \tag{2.52}$$

$$\Phi_{\rm ar}(y) = \int_{x_{\rm min}}^{x_{\rm max}} |B_y(x,y,t=0)|dx. \tag{2.53}$$

The total amount of the initial magnetic flux of the arcade field in the whole region is $\Phi_{\rm ar}$, so that $\Phi_{\rm ar} = 8\Phi_a$ (note that there are four arcades in the simulation box and Φ_a means the amount of flux of one polarity). The values of $\Phi_{\rm pho}$ and $\Phi_{\rm cor}$ in Fig.2.10 are maximum values. We use $\Phi_{\rm cor}$ for Φ_e and $\Phi_{\rm ar}(y_{\rm cor})/8$ for Φ_a for the computation of ζ. The condition expressed by formula (2.47) can well explain the tendency shown in Fig.2.11 by adopting a proper value of κ'. The solid line in Fig.2.11 represents the criterion for formula (2.47) of $\kappa' = 5.0$ for the counter-arranged case and $\kappa' = 4.5$ for the co-arranged case. As shown in Fig.2.11, the condition expressed by formula (2.47) can well explain the results of parameter surveys for CA-type eruptions originating from both the co-arranged and counter-arranged arcades.

The reduction of κ' for the co-arranged case compared with the counter-arranged

case can be interpreted as follows. Because of the diffusion (reconnection) with the emerging flux, the co-arranged arcade loses its magnetic energy during compression, which leads to a reduction in its magnetic pressure. This means the co-arranged arcade is more easily compressed, and reconnection inside the arcade is more easily triggered, compared with the counter-arranged arcade.

Fig.2.7 shows that, when the magnetic scale height a is large, eruptions are more likely to occur. When a is large, the current density is high, causing the initial drift velocity v_d to be large. The dependence of κ' on v_d in Eq.(2.48) shows that eruptions are more likely to occur when v_d is large because of the low value of κ'. Therefore, the obtained model can also qualitatively explain the simulation results regarding the magnetic scale height a.

In a three-dimensional case, it is probable that larger values of κ are required because the radius of expanded emerging flux is smaller than that in a two-dimensional case. In fact, the magnetic field strength of the emerging flux that caused an eruption in Notoya (2006) was twice as large as that in our results. In their simulations, the length scale of a filamentary structure was almost the same size as the emerging flux, and the filamentary structure erupted immediately after forming. This size and time scale more suitably explains the miniature filament eruptions than that of the quiescent filament eruptions (quantitative comparison is in later subsection).

2.4.2 Conditions for RC-Type Eruptions

When the emerging flux is located too close to the PIL, the emerging flux expands the arcade rather than compressing it. Hence, CA-type eruptions are not likely to occur. In the case of counter-arranged arcades, some plasmoids are formed through reconnections in the long current sheet between the arcade and the emerging flux.

The reconnection coupling, the linkage of outflow of one reconnection to inflow of another reconnection, enables a plasmoid to erupt. The formation of small plasmoids is always seen in the current sheet between the arcade and the emerging flux. On the other hand, it is not always predictable from our simulations whether the plasmoids will grow to large plasmoids or not. In addition, when reconnection coupling does not occur, an eruption does not occur, even if there is a continuous growth of a plasmoid. The tendency seen in the results of the parameter survey (Fig.2.6) indicates that RC-type eruptions occur only when the field strength of the emerging flux B_e is small. This is because the reconnection coupling is likely to occur when the two reconnection points are close enough to link with each other. The distance between the two reconnection points depends on the expansion radius of the emerging flux, so that a smaller field strength of emerging flux is preferable. When the location of the emerging flux surrounds the PIL of the co-arranged arcade, no current sheet forms between the arcade and emerging flux, resulting in an 'unformed' case.

RC-type eruptions and 'reversed shear' (RS)-type eruptions, as observed in Kusano et al. (2012), occur under similar conditions. Our simulations reveal that the eruptions are likely to occur when the magnetic scale height a is large (Fig.2.7). Kusano et al. (2012) revealed that their RS-type eruptions are triggered when the shear angle of the arcade is large. As the relation between a and θ is represented in Eq.(2.21), when the width L is constant, larger values of a correspond to larger values of θ, meaning that our parameter dependence on a qualitatively agrees with the results in Kusano et al. (2012). One difference is the formation process of the plasmoids. In RS-type eruptions in Kusano et al. (2004, 2012), the force that causes the magnetic field lines of arcades to converge, by which reconnection is triggered, is the magnetic pressure gradient. In our simulations, the magnetic pressure gradient

is immediately balanced with the gas pressure gradient. Instead of the pressure gradient, the convergence of field lines is enhanced by the coupling of multi-point reconnections in our RC-type eruptions.

In our two-dimensional simulations, the effects of the kink and torus instabilities (Kliem et al., 2004; Török & Kliem, 2005; Kliem & Török, 2006; Fan & Gibson, 2007) are absent. If the torus instability were present, the tendency seen in RC-type eruptions in Fig.2.7 would likely be the opposite because the critical condition of the torus instability is $-d\ln B_{\rm ext}/d\ln R \geq n_{\rm cr}$, where $B_{\rm ext}$ is the external magnetic field strength, R is radius, $n_{\rm cr}$ is critical value, and $n_{\rm cr} \approx 2$ (Kliem & Török, 2006). For the arcade field in our simulations, the critical condition of the torus instability is likely to be

$$\frac{y}{a} \geq n_{\rm cr}. \tag{2.54}$$

Eq.(2.54) shows that the torus instability is likely to be triggered when the magnetic scale height a is small (when the shear angle θ is small). The critical height for the torus instability in our simulations is around $y \approx 2a$. This is much higher than the location where the plasmoid is formed. Therefore, arcades of lower height will be required. The decreasing rate of the field strength along the radial axis in spherical coordinates is larger than that along the vertical axis in Cartesian coordinates, so the torus instability may play an important role in our RC-type mechanism. For a more detailed comparison, we have to perform three-dimensional simulations.

2.4.3 Formed Case

Formed (but non-eruptive) cases are shown with triangles in Fig.2.6 and Fig.2.11, especially at the inner regions of the arcade field. The formed cases lie in the interval between the region where CA-types are dominant and where RC-types are dominant

in the parameter space of χ. One reason why eruptions fail is an interruption of reconnection by dense plasmas. The dense plasma comes from the 'dense sheath', i.e., the top region of the emerging flux. It prevents an increase in the drift velocity, even if the current density increases from compression of the arcade field, leading to a stop in the reconnection. The other reason eruptive magnetic configurations fail is due to the two reconnections failing to couple. Even when the plasmoids grow sufficiently, they do not erupt but remain stationary without the reconnection coupling. The continuous growth of plasmoids in formed cases might lead to eruptions in three-dimensional simulations by the help of the kink or torus instability.

2.4.4 Comparison with Observations

Feynman & Martin (1995) first showed in their statistical study that eruptions were triggered when the spatial arrangement of pre-existing arcade fields and newly emerging flux was favorable for reconnection. In our results, the tendency of the RC-type mechanism is clearly consistent with their observation. In the case of CA-types, both favorable and unfavorable reconnection arrangements can cause eruptions. This is because the most essential point for CA-type eruptions is whether or not the arcade field is compressed enough to cause reconnection. Xu et al. (2008) statistically investigated the triggering mechanism of eruptions caused by emerging flux, especially with respect to the amount and the location of emerging flux. Our simulation results are qualitatively consistent with their study.

The length scale of a filamentary structure in our simulations (here we regard a plasmoid as a filament by taking into account the axial component of its magnetic field) is mostly the same as the spatial scale of emerging flux, which is roughly 18000 - 30000 km. This corresponds to the typical size of miniature filaments, which was

reported by Wang et al. (2000) to have an average value of 19000 km. Moreover, the time frame from formation to eruption of a plasmoid in our simulations is about 30 minutes, which agrees with the mean lifetime of miniature filaments, reported to be 50 minutes. The mean ejection speed varies from 12 km/s to 51 km/s in our simulations, and this also agrees with the observed mean ejection speed of 13 km/s. While not all the miniature filament eruptions are caused by the emerging flux, our model has the potential to explain them.

2.5 SUMMARY

The mechanisms of eruptions associated with interaction between newly emerging flux and coronal arcade fields were investigated by 2.5-dimensional MHD simulations. We found that two possible eruptive mechanisms exist, and we determined their degree of dependence on the parameters of magnetic scale height of the arcade field, the amount of flux, and the location of emerging flux. The CA-type mechanism is dominant when the location of emerging flux surrounds the edges of arcades. This type shows a linear tendency which can be represented as formula (2.47), namely, the formation and eruption of a plasmoid occurs when the location of emerging flux is close to the arcade field and the amount of flux introduced into the corona is large enough. The eruptions are also likely to occur when the magnetic scale height is large (this is the same situation as when the arcade is strongly sheared). The RC-type mechanism is dominant when emerging flux surrounds the PIL. The parameter dependence shows that eruptions are likely to occur when a small amount of magnetic flux is introduced and when the arcade is strongly sheared. In three-dimensional cases, the kink or torus instability may help these types of eruptions.

The results of our parameter survey are qualitatively consistent with previous

observational studies (Feynman & Martin 1995, Xu et al. 2008) and agree quantitatively with the observed physical values of miniature filament eruptions. We conclude that our model has the potential to predict eruptions when the shear angle of the arcade field, the ratio of magnetic flux, and the location of emerging flux relative to the arcade field are observed.

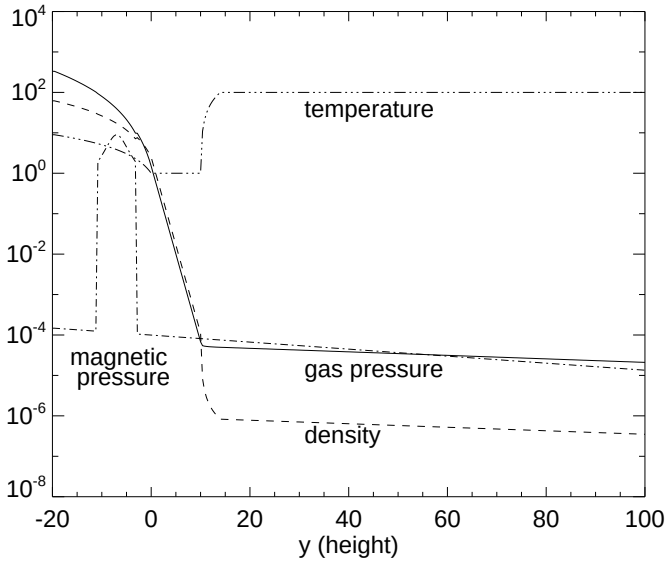

Figure 2.1: Initial vertical distribution of each physical value. Magnetic pressure is plotted in the case of $B_e = 15$.

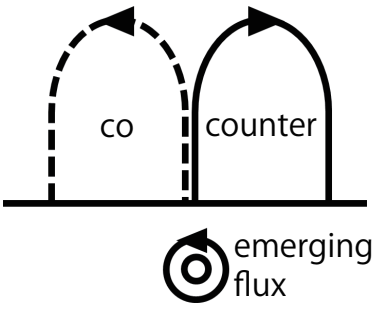

Figure 2.2: Positions of co-arranged and counter-arranged arcade fields. Dashed arcade is co-arranged, and solid arcade is counter-arranged.

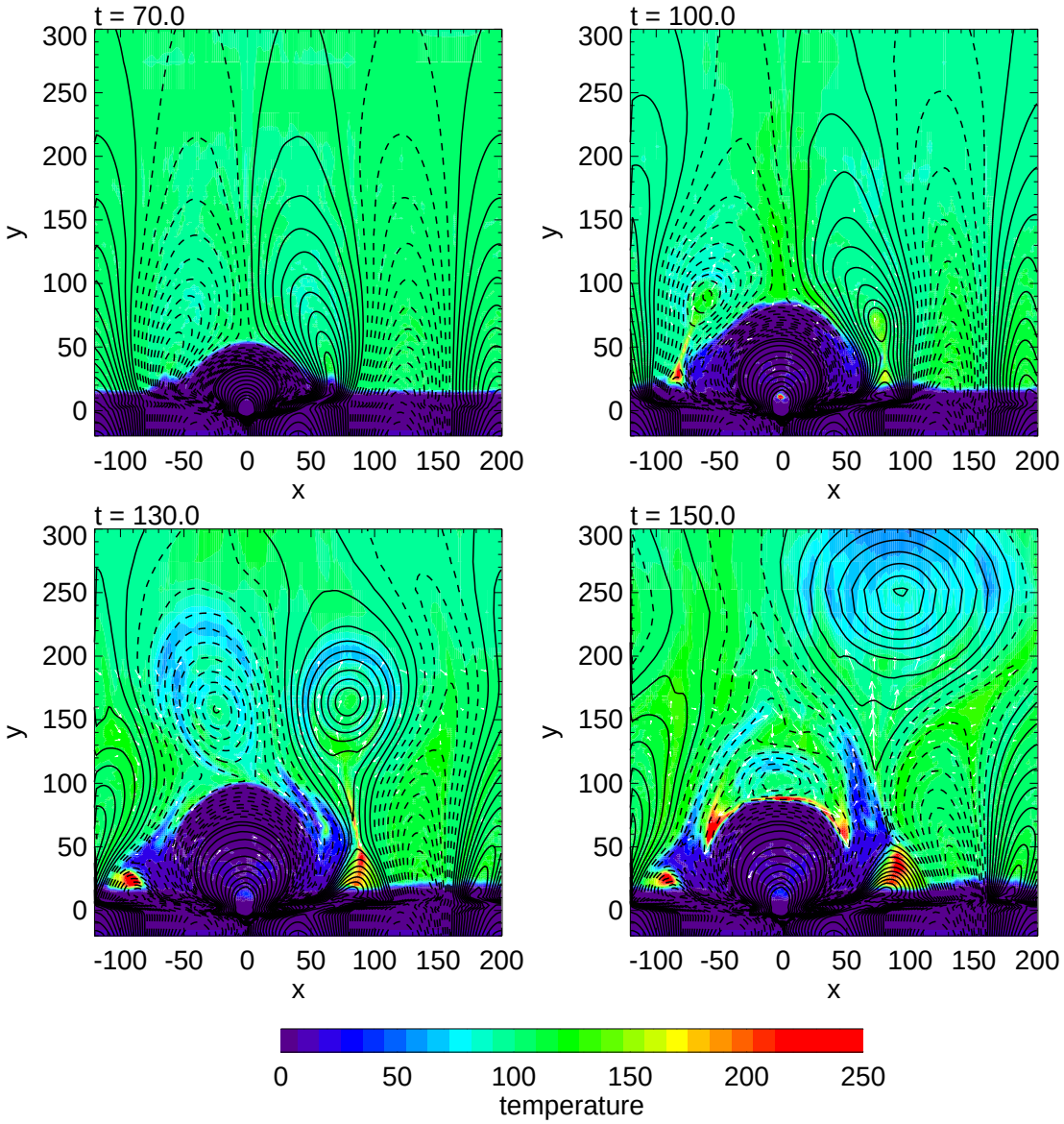

Figure 2.3: Example of CA-type mechanism. Time Evolution of $(B_e, x_e) = (15, 0)$. Magnetic field lines of counter-arranged and co-arranged arcades are represented with solid and dashed lines, respectively. Color represents temperature. This figure is also available as mpeg animation in the electronic edition of the *Astrophysical Journal*.

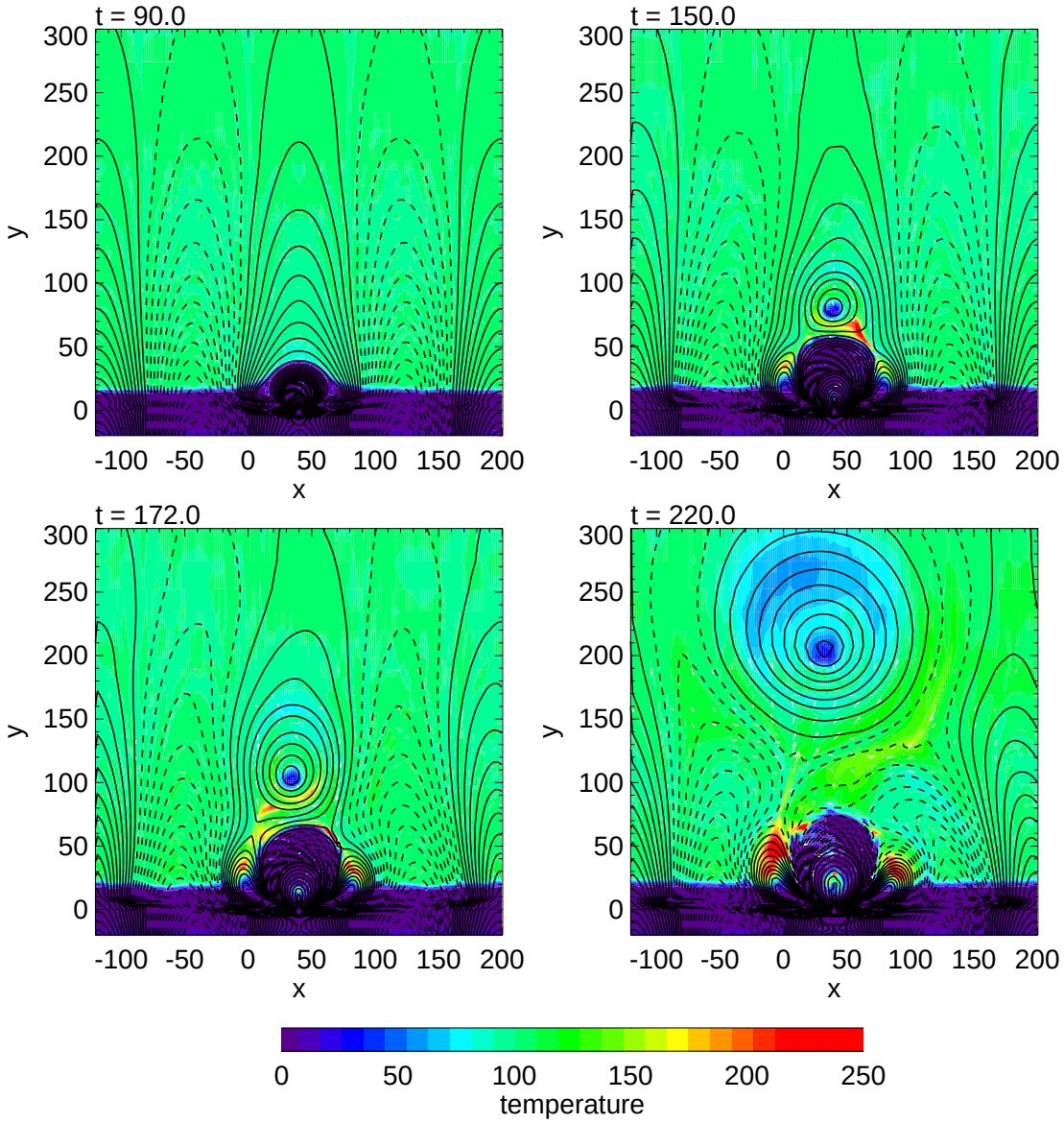

Figure 2.4: Example of RC-type mechanism. Time Evolution of $(B_e, x_e) = (11, 40)$. Magnetic field lines of counter-arranged and co-arranged arcades are represented with solid and dashed lines, respectively. Color represents temperature. This figure is also available as mpeg animation in the electronic edition of the *Astrophysical Journal*.

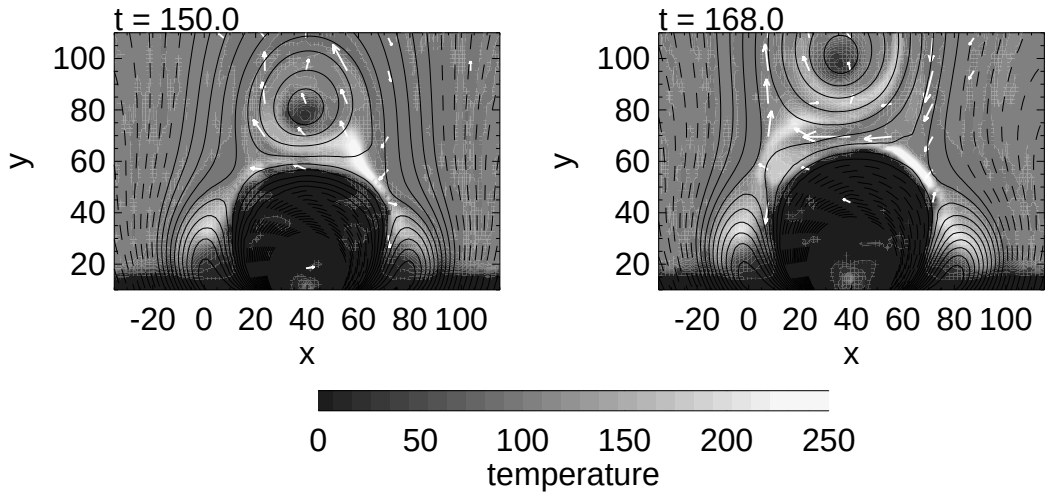

Figure 2.5: Example of reconnection coupling in case of $(B_e, x_e) = (11, 40)$. White arrows represent velocity field. Filled contour represents temperature. Solid and dashed lines are magnetic fields. The outflow from the right reconnection point ($(x, y) = (70, 55)$) passes through the boundary between the arcade and the emerging flux and and links to the inflow region of the left reconnection point ($(x, y) = (5, 60)$).

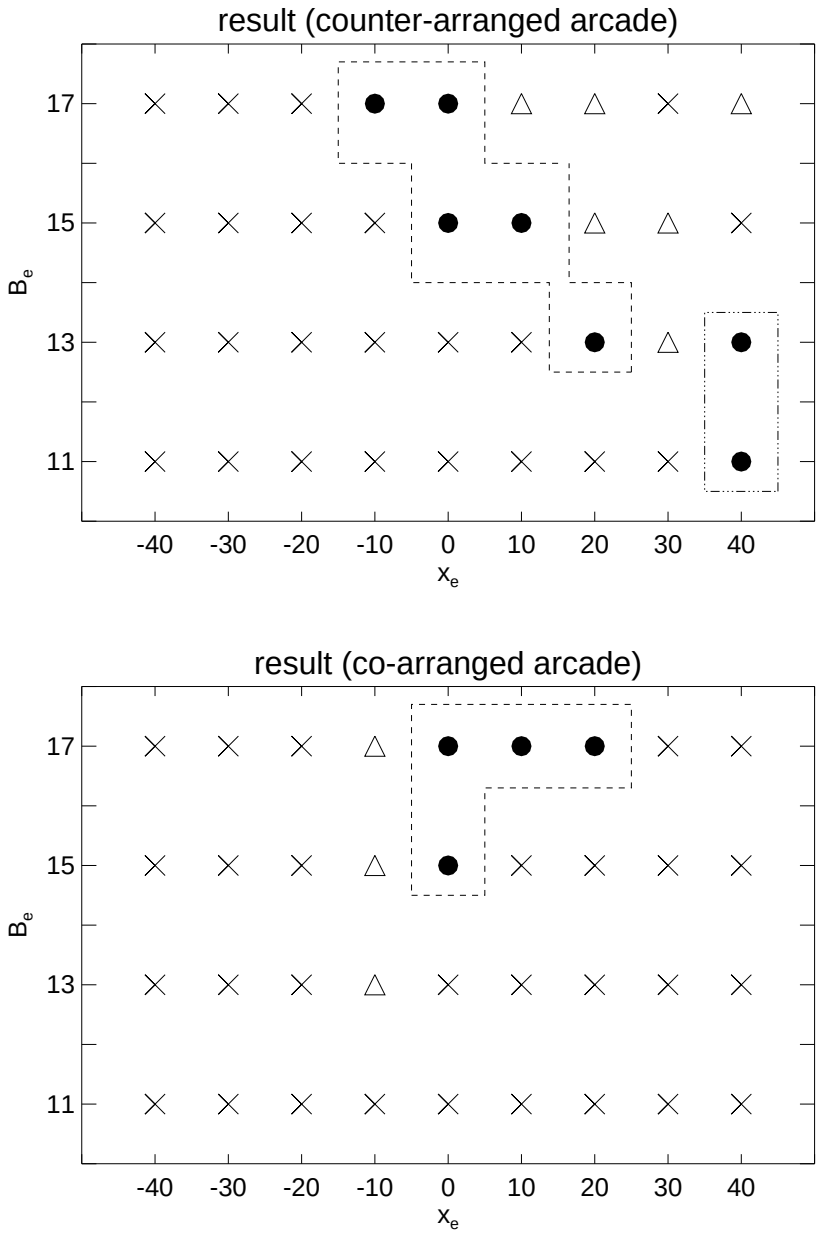

Figure 2.6: Results of parameter survey on field strength B_e and location of emerging flux x_e. The upper panel shows results of the counter-arranged arcade and the lower panel shows results of the co-arranged arcade. Circles are 'erupted', triangles are 'formed', and crosses are 'unformed' cases. Circles in dashed boxes represent CA-type eruptions and those in dot-dashed boxes represent RC-type eruptions.

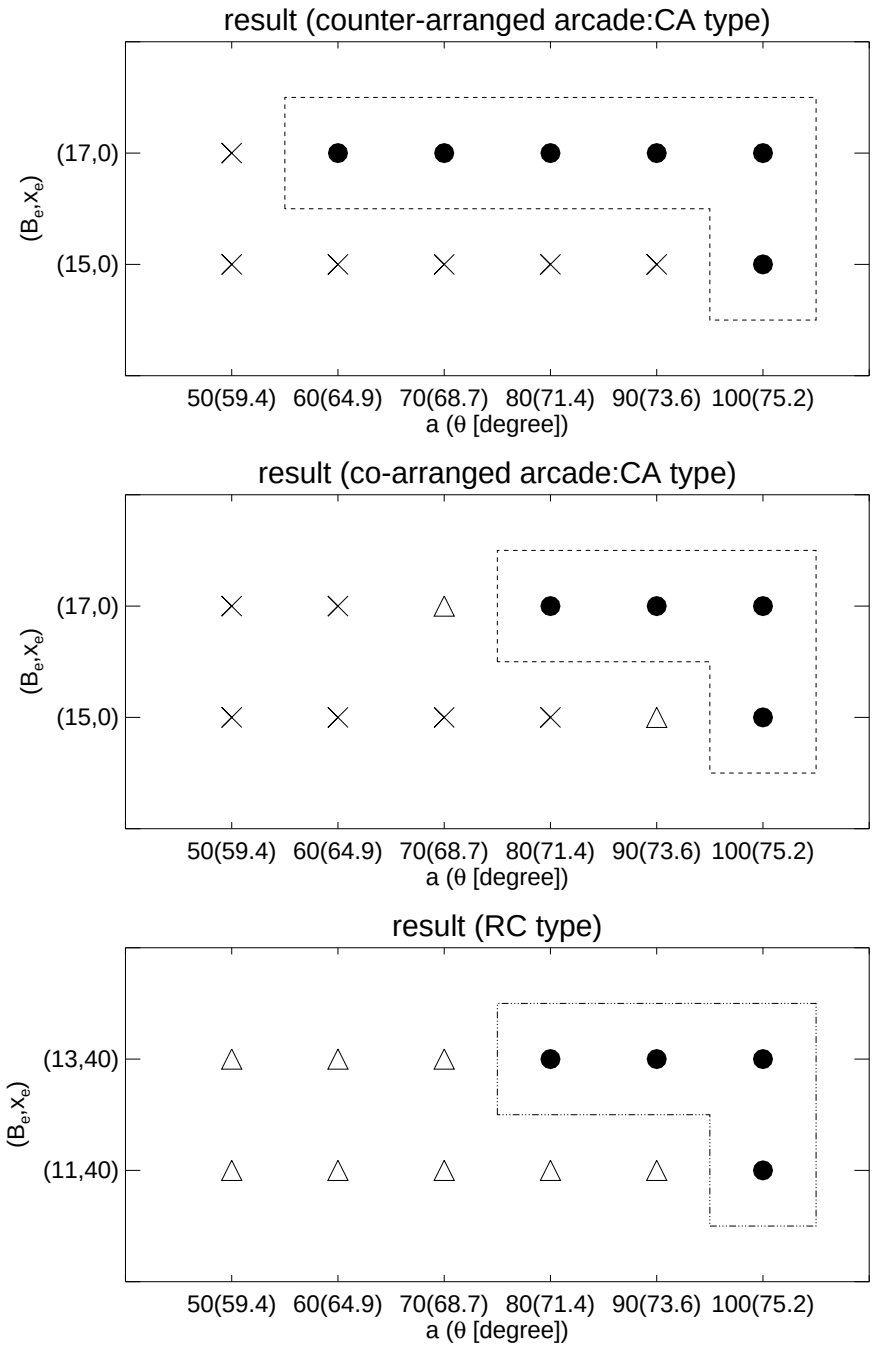

Figure 2.7: Results of parameter survey on magnetic scale height of the arcade field a. Each value of a corresponds to the value of θ in brackets. Circles are 'erupted', triangles are 'formed', and crosses are 'unformed' cases. The top panel shows the results of CA-type eruptions of counter-arranged arcades, and the middle panel shows results of CA-type eruptions or co-arranged arcades. The bottom panel shows the results of RC-type eruptions. Note that RC-type eruption cans be seen only in counter-arranged arcades.

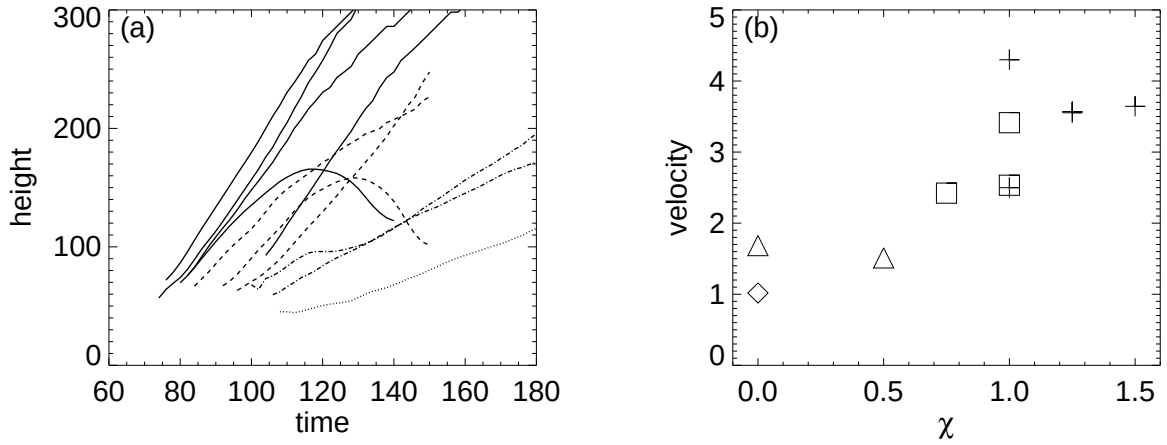

Figure 2.8: (a): Time evolution of height of the plasmoid in each eruptive case. Solid lines represent $B_e = 17$ cases, dashed lines represent $B_e = 15$ cases, dot-dashed lines represent $B_e = 13$ cases, and the dotted line represents $B_e = 11$ case. Plasmoids originating from co-arranged arcades are prevented from rising by the downward magnetic tension force of arcades, resulting in falling down (corresponds to two falling down cases in the figure). (b): mean ejection speed of the plasmoid in each eruptive case. Crosses(+) represent $B_e = 17$ cases, squares(□) represent $B_e = 15$ cases, triangles(△) represent $B_e = 13$ cases, and diamonds(◇) represent $B_e = 11$ case.

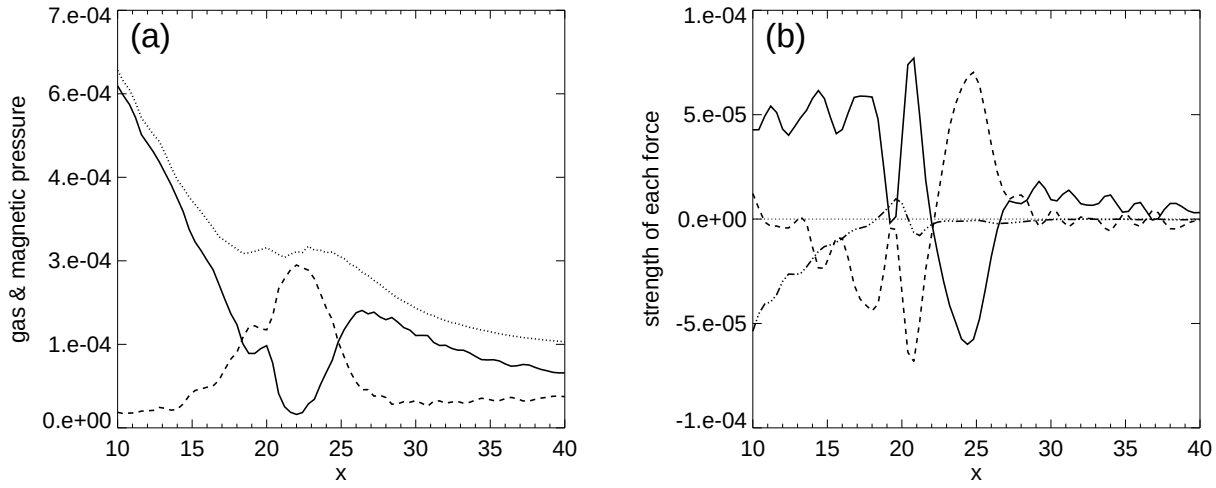

Figure 2.9: (a): Pressure in the vicinity of emerging flux. Solid line is magnetic pressure, dashed line is gas pressure and dotted line is total pressure. (b): x-directional forces at the same region as (a). Solid line is magnetic pressure gradient, dashed line is gas pressure gradient and dot-dashed line is magnetic tension force.

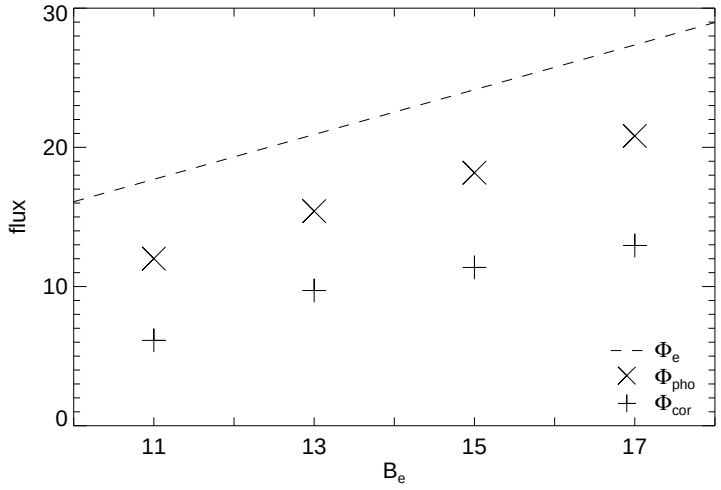

Figure 2.10: Amount of magnetic flux injected into photosphere and corona. $\times$ is $\Phi_{\rm pho}$ and $+$ is $\Phi_{\rm cor}$. Dashed line represents the initial magnetic flux of a tube.

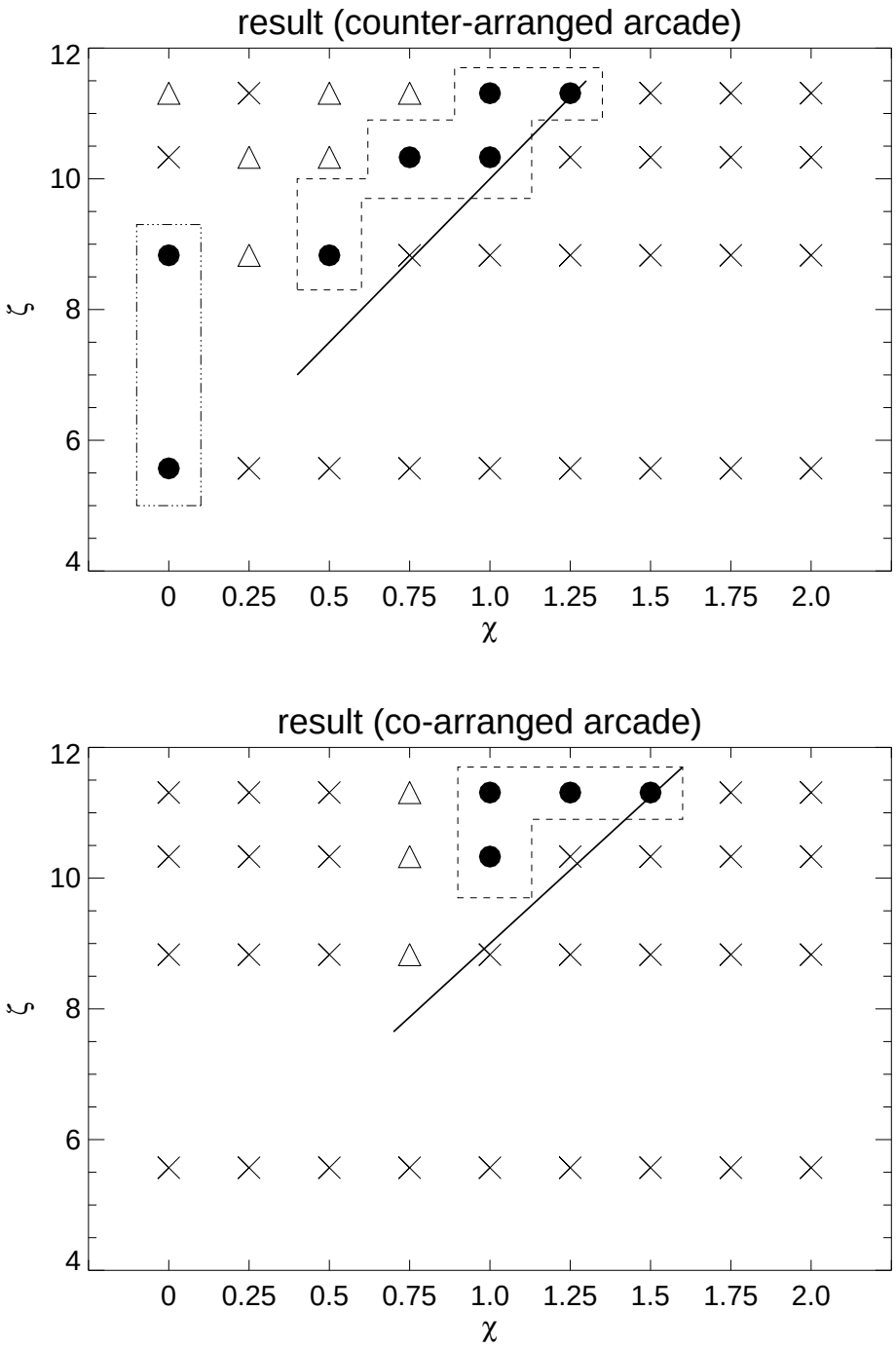

Figure 2.11: Results of parameter survey of counter-arranged arcades (upper panel) and co-arranged arcades (lower panel). Circles are 'erupted' cases, triangles are 'formed' cases, and crosses are 'unformed' cases. $\chi \leq 1.0$ is inner arcade region and $\chi \geq 1.0$ is outer arcade region. Circles in dashed boxes represent CA-type eruptions and those in dot-dashed boxes represent RC-type eruptions. Solid lines represent the eruptive condition expressed by formula (2.47).

Chapter 3

Filament Formation by Thermal Instability

3.1 Introduction

Solar filaments are cool dense plasma clouds in the hot tenuous corona. The dense plasmas are sustained at the dip, concave-up structure, of coronal magnetic fields. One candidate to explain the origin of filaments' cool dense plasmas is the evaporation-condensation model (Antiochos & Klimchuk, 1991). This model is based on the theory of the thermal instability (Field, 1965) and the thermal stability of coronal loops (Rosner et al., 1978). Antiochos & Klimchuk (1991) verified that the thermal instability is triggered by introducing the heating whose scale length is small enough compared with the loop length and which is localized at the footpoints. The localized heating causes the chromospheric evaporation and makes the coronal loop thermally unstable by injecting hot dense plasmas. Because of the radiative cooling function which has negative inclination against the temperature above 3×10^5K, the catastrophic temperature decrease and density increase are caused around the

midpoint of the loop, leading to the formation of cool dense plasma blobs (condensations) in the corona. The constraints on the parameters of the localized heating and the geometry of the loop are given by one-dimensional hydrodynamic simulations. (Antiochos et al., 1999; Karpen et al., 2001, 2003, 2005; Karpen & Antiochos, 2008; Luna et al., 2012).

The observations by Berger et al. (2012) gave a support for the condensation process. It was the polar crown filament located inside the coronal cavity, which is a darker region than the surrounding corona and represents the magnetic flux rope structure in the corona (Low & Hundhausen, 1995; BĄk-Stęślicka et al., 2013). Their analysis of multi-wavelength data sets from SDO/AIA indicate the condensation process due to radiative cooling, while the evidence of the evaporation is still absent in the observations.

The filament observed by Berger et al. (2012) would have the flux rope structure. In general, the magnetic structure of a filament can be categorized into two models. One is the Kippenhaln-Schlüter model (Kippenhahn & Schlüter, 1957) in which the basic magnetic structure is the arched system and the dip structure is formed by the weight of condensations (hereafter, the KS model). The other is the Kuperus-Raadu model (Kuperus & Raadu, 1974) in which the dip is a part of a twisted loop-like magnetic structure (hereafter, the KR model). The flux rope structure belongs to the KR model. These two models are discriminated by the magnetic polarity: it is same as that of the overlying arcade field (normal polarity) in KS model, while it is opposite (inverse polarity) in KR model. Both normal and inverse polarity filaments are observed in the solar atmosphere (Leroy et al., 1984).

Xia et al. (2012) demonstrated the evaporation-condensation model by self-consistent MHD simulations including thermal conduction, radiative cooling, and

gravity, and succeeded in reproducing the filament of the KS model . On the other hand, the model to reproduce the filament of the KR model with condensation process is still not established. In the frame of the evaporation-condensation model, the magnetic structure maintains normal polarity associated with the arched structure, and does not reproduce inverse polarity associated with the flux rope structure.

In this chapter, we propose a new idea to reproduce the filament of the KR model with the condensation process, which is triggered by the formation of a flux rope instead of the chromospheric evaporation, and demonstrate it by 2.5-dimensional (two-dimensional space with three vector components) self-consistent MHD simulations.

In §3.2, we propose our new model. In §3.3, numerical settings to demonstrate the model is described. The results are shown in §3.4 and the process to form condensation is discussed in §3.5. §3.6 is summary of this chapter.

3.2 Levitation-condensation model

We propose the new model named levitation-condensation model. This model uses the formation of a flux rope instead of chromospheric evaporation . At first, the corona is under thermal equilibrium (Fig.3.1(a)). The flux rope structure is formed by two distinct ways, one is the converging motion (van Ballegooijen & Martens, 1989; Martens & Zwaan, 2001), the other is the interaction between the emerging flux and the arcade field (RC type mechanism with weak emerging flux in Chapter 2). The dense plasmas at the lower corona is trapped inside the closed loops and lifted up to the upper corona during the formation of the flux rope, where 'closed loops' means the magnetic loop detached from the bottom boundary (Fig.3.1(b)). The models in which the dense plasmas are lifted up by rising magnetic fields are named

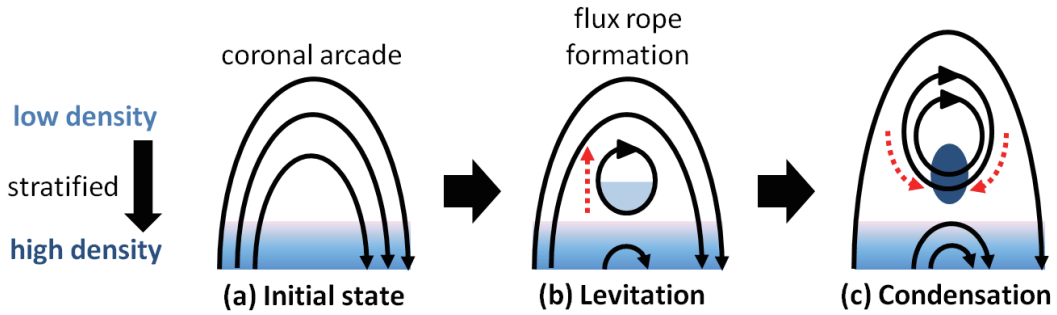

Figure 3.1: Schematic drawings of levitation-evaporation model. Thin black arrows represent magnetic field lines. Red lines represent motion of plasma.

'levitation models' (Mackay et al., 2010). The thermal imbalance is caused inside the flux rope by the increased radiative cooling due to the dense plasma. Because the closed field lines connect to nowhere, the decrease in temperature inside the flux rope does not conduct outwards. Consequently, the thermal instability (or the thermal collapse) is triggered (Fig.3.1(c)).

3.3 Numerical settings

3.3.1 Basic equations and numerical scheme

We solve nonlinear, time-dependent, resistive, compressible MHD equations including thermal conduction along the magnetic field lines, radiative cooling, and gravity in a two-dimensional space. The equations are

$$\frac{\partial \rho}{\partial t} + \boldsymbol{v} \cdot \boldsymbol{\nabla} \rho = -\rho \boldsymbol{\nabla} \cdot \boldsymbol{v} \tag{3.1}$$

$$\frac{\partial p}{\partial t} + \boldsymbol{v} \cdot \boldsymbol{\nabla} p = -\gamma p \boldsymbol{\nabla} \cdot \boldsymbol{v} + \boldsymbol{\nabla} \cdot (\kappa \boldsymbol{b}\boldsymbol{b} \cdot \boldsymbol{\nabla} T) - (\gamma - 1)\, L \tag{3.2}$$

$$\frac{\partial \boldsymbol{v}}{\partial t} + \boldsymbol{v} \cdot \boldsymbol{\nabla} \boldsymbol{v} = -\frac{1}{\rho} \boldsymbol{\nabla} p + \frac{1}{4\pi\rho} (\boldsymbol{\nabla} \times \boldsymbol{B}) \times \boldsymbol{B} + \boldsymbol{g} \tag{3.3}$$

$$\frac{\partial \boldsymbol{B}}{\partial t} = -c \boldsymbol{\nabla} \times \boldsymbol{E} \tag{3.4}$$

$$\boldsymbol{E} = -\frac{1}{c} \boldsymbol{v} \times \boldsymbol{B} + \frac{4\pi\eta}{c^2} \boldsymbol{J} \tag{3.5}$$

$$\boldsymbol{J} = \frac{c}{4\pi} \boldsymbol{\nabla} \times \boldsymbol{B} \tag{3.6}$$

$\boldsymbol{g} = (0, -g_{\rm cor})$ is the gravitational acceleration, $g_{\rm cor} = 2.7 \times 10^4$ cm s^{-2}. Temperature is derived from the equation of state:

$$T = \frac{m}{k_B} \frac{p}{\rho} \tag{3.7}$$

where m is the mean molecular mass (assumed constant), and k_B is the Boltzmann's constant. The second term of the right hand side in Eq.(3.2) represents the Spitzer type thermal conduction (Spitzer, 1962), where $\kappa = 2 \times 10^{-6}$ erg cm^{-1} s^{-1} K$^{-7/2}$ is the coefficient of the thermal conduction, $\boldsymbol{b}$ is a unit vector along the magnetic field, and by which heat is conducted only along the magnetic field lines. The third term of the right hand side in Eq.(3.2) represents net cooling rate. The setting of the net cooling L is described later. η is the magnetic diffusion rate. In order to reproduce the fast reconnection in the solar atmosphere, whose time scale is several hundred seconds, we use the Petschek-type reconnection (Petschek, 1964) which is triggered by the localized diffusion region. It is confirmed that the Petschek-type reconnection is triggered by introducing anomalous resistivity (e.g Yokoyama & Shibata, 1994) in the numerical simulations. We adopt the following form of the anomalous resistivity,

$$\eta = \begin{cases} 0 & (J < J_c) \qquad (3.8) \\ \eta_0 \left(J/J_c - 1 \right)^2 & (J \geq J_c) \qquad (3.9) \end{cases}$$

where $\eta_0 = 3.6 \times 10^{13}$ cm^2 s^{-1}, $J_c = 25$ dyn$^{1/2}$ cm s^{-1}. We restrict the value of η to $\eta_{\max} = 18.0 \times 10^{13}$ cm^2 s^{-1}. This artificial resistivity is only for reproducing the localized diffusion region, which must be well resolved by the given grid size. Even though the magnitude is much larger than the value in the corona $\eta = 10^4$ cm^2 s^{-1} which is derived by Spitzer (1962), the reconnection heating rate is negligible compared with the background heating rate (checked later).

The net cooling term is expressed as

$$L = n^2\Lambda(T) - H, \tag{3.10}$$

where n is number density, $\Lambda(T)$ is radiative loss function of the optically thin plasma, and H is the background heating rate. The simplified model of the radiative loss function (Fig3.2) is used in our simulations. As for heating rate H, because the mechanism of the heating in the corona is still unknown, we assume two types of models. In each model, $L = 0$ in the initial state, hence, the initial state is under the thermal equilibrium. In one model, the heating rate H depends on the local magnetic energy density (magnetic pressure) when the temperature is above the admissible temperature $T_{\rm adm}$, and the net cooling vanishes when the temperature is under $T_{\rm adm}$,

$$L = \begin{cases} n^2\Lambda(T) - \alpha P_m, & (T \geq T_{\rm adm}) \quad (3.11) \\ 0, \quad (T < T_{\rm adm}) & (3.12) \end{cases}$$

where α is constant. The setting represented as Eq. (3.12) is for prohibiting the temperature from decreasing lower than $T_{\rm adm}$. The method to determine the value of $T_{\rm adm}$ is described in the subsection 3.3.3. In the other model, the heating rate H depends on the local density and the height when the temperature is above $T_{\rm adm}$,

and the net cooling vanishes under the temperature of $T_{\rm adm}$,

$$L = \begin{cases} n^2\Lambda(T) - \alpha(y)\rho, & (T \geq T_{\rm adm}) \quad (3.13) \\ 0, & (T < T_{\rm adm}) \quad (3.14) \end{cases}$$

where α depends on the height y because of the initial thermal equilibrium.

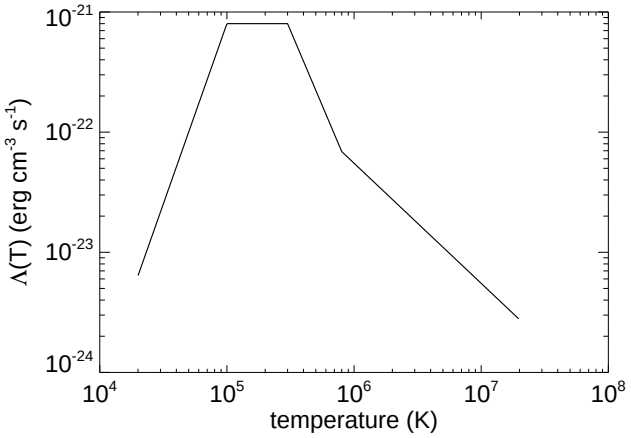

Figure 3.2: Simplified radiative loss function

3.3.2 Initial condition and boundary condition

We set the model of the corona in a rectangular calculation box, in which x-axis is horizontal, the y-axis is vertical, and z-axis is orthogonal to the x-y plane. The corona is stratified under a uniform temperature ($T_{\rm cor} = 1$MK) and gravity ,

$$n(y) = n_{\rm cor} \exp\left[-\frac{mg_{\rm cor}}{k_B T_{\rm cor}} y\right], \quad (3.15)$$

$$p(y) = n(y) k_B T_{\rm cor}, \quad (3.16)$$

where $n_{\rm cor} = 2 \times 10^9$ cm^{-3}. The typical density of the active region is order of 10^9 cm^{-3}, while that of the quiet region is 10^8 cm^{-3}. The force-free arcade field represented as follows is set in the box.

$$B_x = -\left(\frac{2L_a}{\pi a}\right) B_a \cos\left(\frac{\pi}{2L_a}x\right) \exp\left[-\frac{y}{a}\right], \tag{3.17}$$

$$B_y = B_a \sin\left(\frac{\pi}{2L_a}x\right) \exp\left[-\frac{y}{a}\right], \tag{3.18}$$

$$B_z = -\sqrt{1-\left(\frac{2L_a}{\pi a}\right)^2} B_a \cos\left(\frac{\pi}{2L_a}x\right) \exp\left[-\frac{y}{a}\right], \tag{3.19}$$

where $B_a = 3$ G, $L_a = 1.2 \times 10^4$ km, and $a = 3.1 \times 10^4$ km. Fig.3.3 shows the initial state. The magnetic field strength of the quiescent filaments is $3 - 15$G, while that of the active region filaments is $30 - 45$ G. $B_a = 3$ G is small compared with the active region density $n_{\rm cor} = 2 \times 10^9$ cm^{-3} or the density is high compared with the field strength. The aim of this study is reproducing the filament of the KR model, so that we overlook the mismatch between the field strength and the density, and choose the values for reducing the calculation amount.

The symmetry or antisymmetry boundary condition is applied to the left and right boundaries. The symmetry boundary condition is applied to ρ, p, v_y, B_y and the antisymmetry boundary conditions is applied to v_x, v_z, B_x, B_z. By applying the temporally varying boundary condition to the bottom boundary, two types of the mechanisms for forming a flux rope are tested: one is the converging motion, the other is interaction between the emerging flux and the arcade field (see Fig.3.4). In the case of the converging motion, the velocity of the bottom boundary $\boldsymbol{v}^b$ is set as

follows,

$$v_x^b = v_z^b = v_0(t)\frac{x}{L_a/4},\ v_y^b = 0, \quad (0 \le x < L_a/4) \tag{3.20}$$

$$v_x^b = v_z^b = v_0(t)\frac{(L_a - x)}{3L_a/4},\ v_y^b = 0, \quad (L_a/4 \le x \le L_a) \tag{3.21}$$

where

$$v_0(t) = \begin{cases} -12 \text{ km/s}, \quad (t < 1000s) & (3.22) \\ -12(1500 - t)/(1500 - 1000) \text{ km/s}, \quad (1000s \le t < 1500s) & (3.23) \\ 0. \qquad (t \ge 1500s) & (3.24) \end{cases}$$

The magnetic field on the bottom boundary $\boldsymbol{B}^b$ is derived from the induction equation,

$$\boldsymbol{B}^{b,\mathrm{N}+1} = \boldsymbol{B}^{b,\mathrm{N}} + \Delta t \boldsymbol{\nabla} \times (\boldsymbol{v}^b \times \boldsymbol{B}^{b,\mathrm{N}}), \tag{3.25}$$

where the superscript N denotes the time step. In the case of the emerging flux, the velocity $\boldsymbol{v}^b$ is set as follows,

$$v_y^b = v_0\frac{1 + \tanh(r_e - x)}{2},\ v_x = v_z = 0 \tag{3.26}$$

where $r_e = 1.2 \times 10^3$ km, and

$$v_0(t) = \begin{cases} 2.4 \text{ km/s} \quad (t < 250s) & (3.27) \\ 0.0 \quad (t \ge 250s) & (3.28) \end{cases}$$

The magnetic field on the bottom boundary $\boldsymbol{B}^b$ is derived from

$$\boldsymbol{B}^{b,\mathrm{N}+1} = \boldsymbol{B}^{b,\mathrm{N}} + \Delta t \boldsymbol{\nabla} \times \left(\boldsymbol{v}^b \times \boldsymbol{B}^e(t)\right), \tag{3.29}$$

where $\boldsymbol{B}^e(t)$ is the magnetic field of the emerging flux. $\boldsymbol{B}^e(t)$ is set as follows,

$$B_x^e = -q(y-y_0)B_z^e, \tag{3.30}$$

$$B_y^e = qxB_z^e, \tag{3.31}$$

$$B_z^e = \frac{B_0}{1+q^2r^2}\exp[-(r/r_e)^2], \tag{3.32}$$

$$r = x^2+(y-y_0)^2, \tag{3.33}$$

where $B_0 = 6$ G, $q = 1.7\times10^{-3}$ km^{-1} and

$$y_0 = \begin{cases} -1.95+0.0024t \text{ Mm}, & (t<250s) \quad (3.34) \\ -1.35 \text{ Mm}. & (t>250s) \quad (3.35) \end{cases}$$

The gas pressure and density of the bottom boundary is derived as follows,

$$-\frac{p_{i,j+1}-p_{i,j}}{\Delta y} - \frac{1}{2}\left(\frac{mp_{i,j}}{k_BT_{\rm cor}}+\frac{mp_{i,j+1}}{k_BT_{\rm cor}}\right)g_{\rm cor} = 0, \tag{3.36}$$

$$\rho_{i,j} = \frac{mp_{i,j}}{k_BT_{\rm cor}}, \tag{3.37}$$

where $T_{\rm cor} = 10^6$ K and subscript i and j denotes the x and y coordinate, respectively. By this boundary condition, the temperature of the bottom boundary is kept to be $T_{\rm cor}$.

3.3.3 Numerical scheme and grid size

The numerical scheme is based on CIP-MOCCT method (Kudoh et al., 1999). For the advection part of the equations (the left hand side of Eqs.(3.1)-(3.3)), the Rational CIP scheme (Xiao et al., 1996), in which the rational function instead of the cubic function is adopted for the interpolation function. is used for preventing nu-

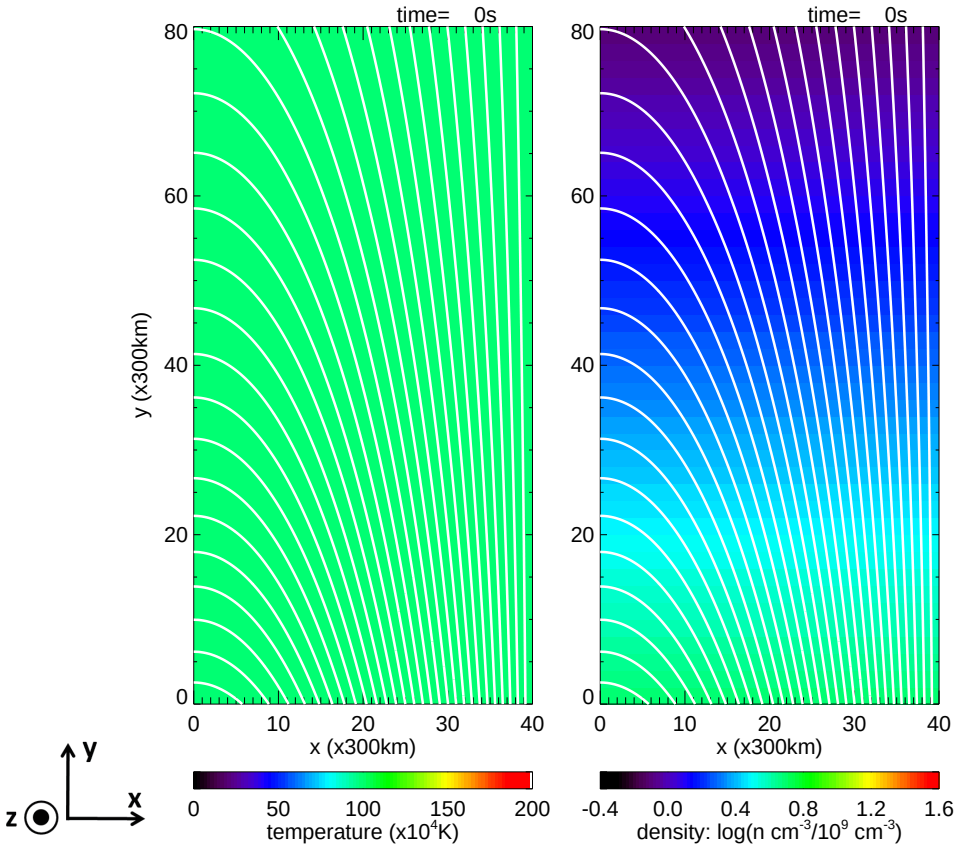

Figure 3.3: Initial state. Colors in the left and right panel represent the temperature and density. White lines represent magnetic field lines.

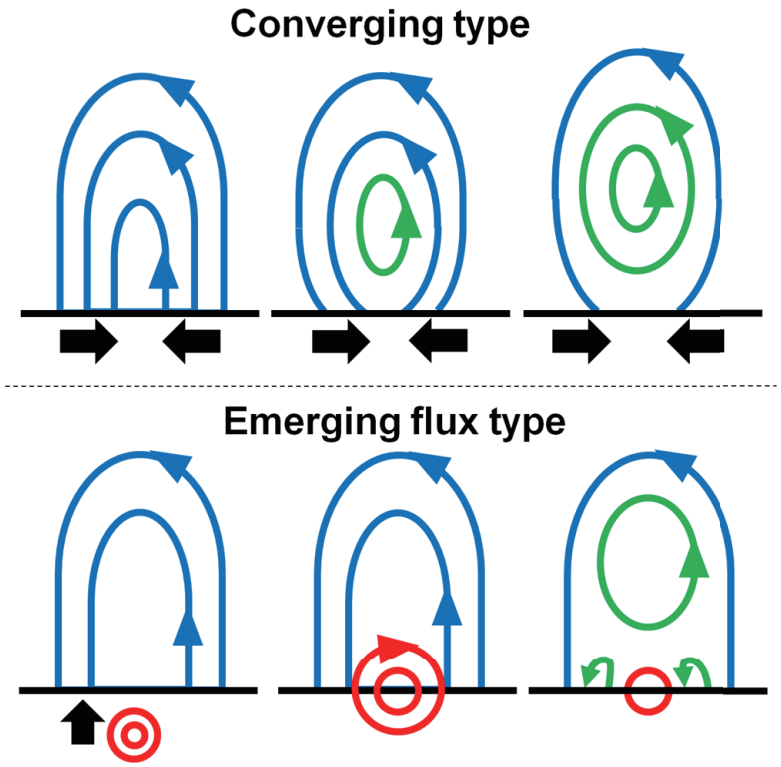

Figure 3.4: Schematic drawings of the formation mechanisms.

merical oscillations. The thermal conduction, radiative cooling and heating terms are included as source terms. The thermal conduction is solved by explicit method.

The required grid size for a simulation of the thermal instability can be computed by the formula in Koyama & Inutsuka (2004). Fig.3.5 shows the grid size of 3km is sufficient to cover whole range of temperature when the radiative loss function is defined as Fig3.2. In order to reduce the calculation amount (to use larger grid size), we apply the technical treatment to heating term and make temperature not to be lower than the admissible value which depends on the grid size as Fig. 3.5. The heating term depends on the local magnetic pressure or the density when the temperature is larger than the admissible temperature $T_{\rm adm}$. When the temperature is smaller than $T_{\rm adm}$, the heating term is set to be balanced with the cooling term. We adopt the grid size of 120, 60, and 30 km. $T_{\rm adm}$ of each grid size is 0.5, 0.4, and 0.3 MK, respectively. The horizontal grid size Δx is uniform. The vertical grid size Δy is uniform in $y < 3.0 \times 10^4$ km and increased to $\Delta y = 1.8 \times 10^3$ km in $y > 3.0 \times 10^4$km in order to set the upper boundary far enough. The size of calculation box is 1.2×10^4 km horizontally and 1.2×10^5 km vertically.

3.3.4 Cases under investigations

We classify the simulation models by the type of heating term and the mechanism for formation of the flux rope. The heating term depends on the local magnetic pressure in case A and B, and depends on the local density in case C and D. The formation mechanism is due to the converging motion in case A and C, and is due to the emerging flux in case B and D.

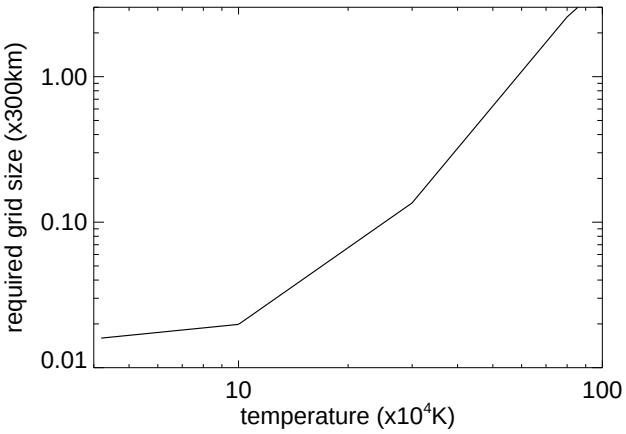

Figure 3.5: Required grid size as a function of temperature

	converging	emerging flux
$H = \alpha P_m$	case A	case C
$H = \alpha \rho$	case B	case D

Table 3.1: Classification of simulation models.

3.4 RESULTS

Fig.3.6 shows the snapshots of time evolution in the case A. Fig.3.7 (a) and (b) shows the time evolution of temperature and density along y-axis, respectively. The levels of each color contour are the same as those in Fig.3.6. The dashed line, the dot-dashed line and the three-dots-dashed line corresponds those in 3.7 correspond that in Fig.3.6. The resolution is $\Delta x = 30$ km and we set $T_{\rm adm} = 0.3$ MK. The flux rope is formed above the PIL of the arcade field by the reconnection which is triggered by the converging motion toward the PIL (time=625 s). As the reconnection proceeds, the relatively dense plasmas which at first exist in the lower corona is trapped inside the flux rope and lifted to the upper corona (levitation process, time=1500 s). Due to the dense plasmas, the radiative cooling in the flux rope overwhelms the background heating, leading to thermal imbalance. Because the thermal conduction works only along the magnetic field line, the suppression of the temperature gradient caused by the thermal imbalance is limited inside the flux rope. By the thermal imbalance and the limitation to the thermal conduction, the thermal instability is triggered inside the flux rope (time=3000 s). The thermal instability forms the cool dense plasmas. The cool dense plasmas go downward along the magnetic field line due to the gravity and accumulates at the lower part of the flux rope, forming the condensation (time=5000 s). Fig.3.8 shows the snapshot of time=7500 s. At this time, the state is quasi-stationary. As seen around $(x, y) = (6000 \text{ km}, 3000 \text{ km})$, a high-density blob is also formed outside of the flux rope. The thermal instability is triggered even in the surrounding field lines which is rooted to the bottom boundary. The formation of this dense part is discussed in Section 3.5. Fig.3.9 shows the distribution of the temperature, the number density, and the magnetic field component B_x along y-axis of time=5000 s. We regard the

cooler and denser region than the initial state as the filament's cool dense plasma. The region of the inverse polarity region is formed in 1200km $< y <$ 10500km where the polarity is opposite to the initial arcade field and the overlying arcade field, corresponding to the KR model.

Fig.3.10 shows the snapshots of time evolution in the case B. Fig.3.11 (a) and (b) shows the time evolution of temperature and density along y-axis, respectively. The thermal instability is triggered with the same process as in the case A. Fig.3.12 shows the distribution of the temperature, the number density, and the magnetic field component B_x along y-axis of time=5000s. The inverse polarity region is formed, hence, the filament of the KR model is also reproduced in the case B. The difference between the case A and the case B is the time scale of the temperature decrease and the density increase in the lower part of the flux rope. After the thermal instability is triggered at the center of the flux rope, the cooling of the lower part is rapid (about 500 s) in the case A, while it is slow (about 2500 s) in the case B.

Fig.3.13 shows the snapshots of time integration in the case C, and Fig.3.14 (a) and (b) shows the time evolution of temperature and density along y-axis, respectively. The flux rope is formed by the interaction between the emerging flux and the arcade field (time=3100 s), and the temperature inside the flux rope gradually decreases due to the strong radiative cooling of the dense plasmas (time=5350 s). After the thermal instability is triggered, the cool dense plasma accumulates at the lower part of the flux rope (time=7875 $-$ 12500s). Though both the formation mechanism of the flux rope and heating type are different, the essential process for the formation of condensation is the same as that in the case A and B. The filaments of the KR model is also reproduced in this case (Fig.3.15).

It is common for all the cases A - D that the thermal instability is triggered inside

the newly formed flux rope and the cool dense plasmas accumulate into the lower part of the flux rope. The polarity of the magnetic field inside the condensation (filament) is opposite to that of the initial and overlying arcade field, hence reproducing the filament of the KR model with condensation process is succeeded in every case.

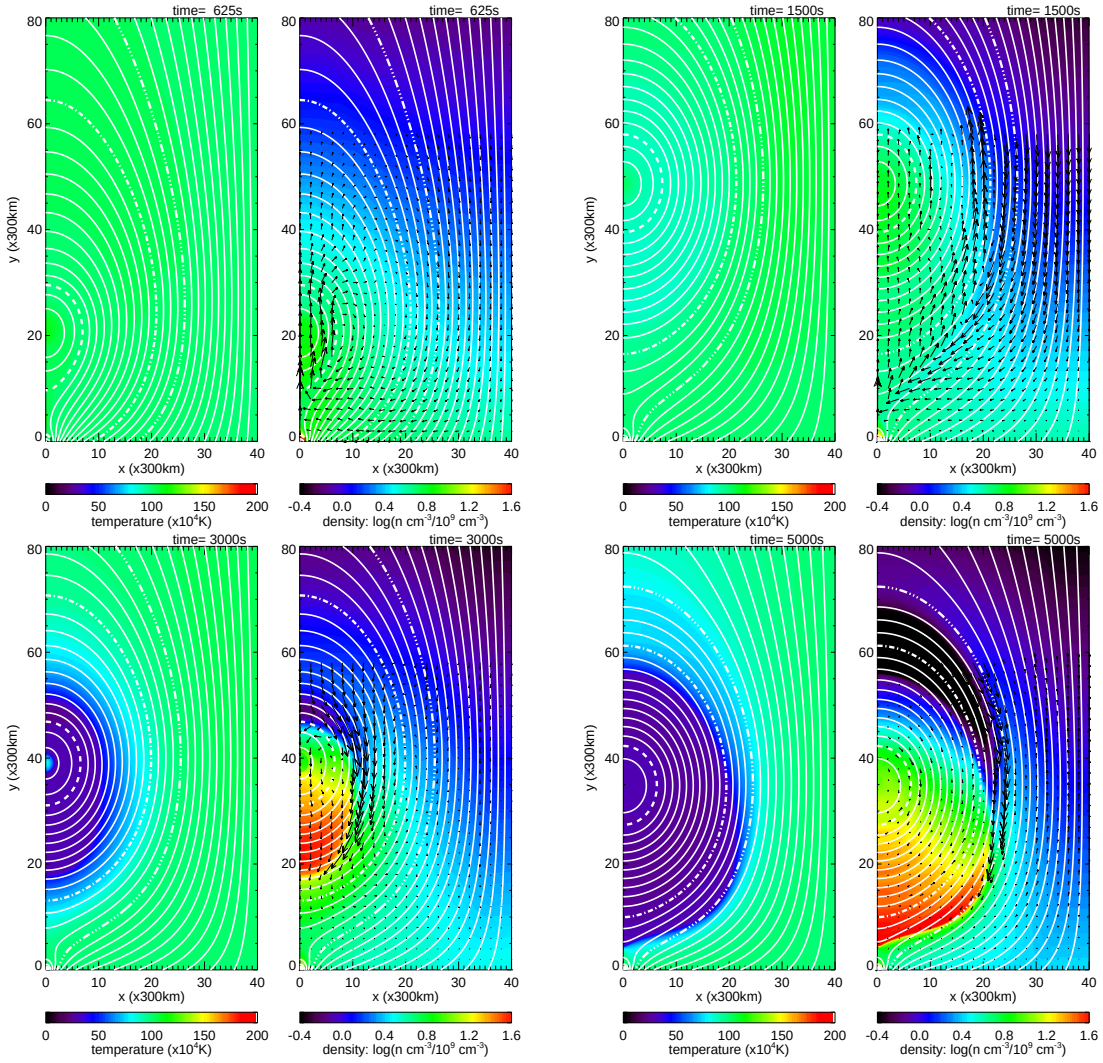

Figure 3.6: Time evolution of formation of flux rope structure and cool dense plasma layer by thermal instability. Colors represent temperature and density. White lines represent magnetic field lines, and arrows represent velocity fields.

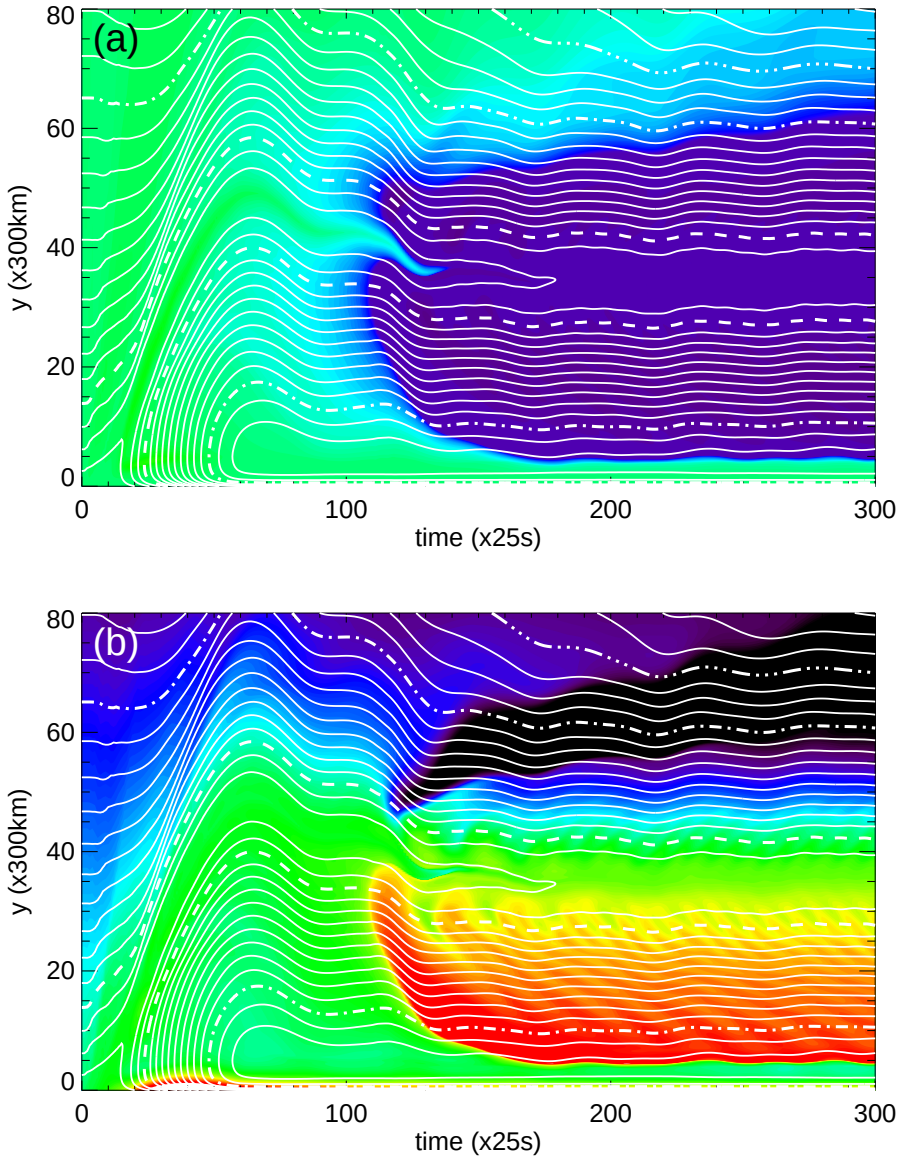

Figure 3.7: Time evolution of temperature and density along y-axis. Colors represent temperature in panel (a) and density in panel (b). Horizontal axis represents time and vertical axis represents height (y). Colors represent density, and white lines represent the positions of magnetic field line. The levels of each contour is the same as those in Fig.3.6

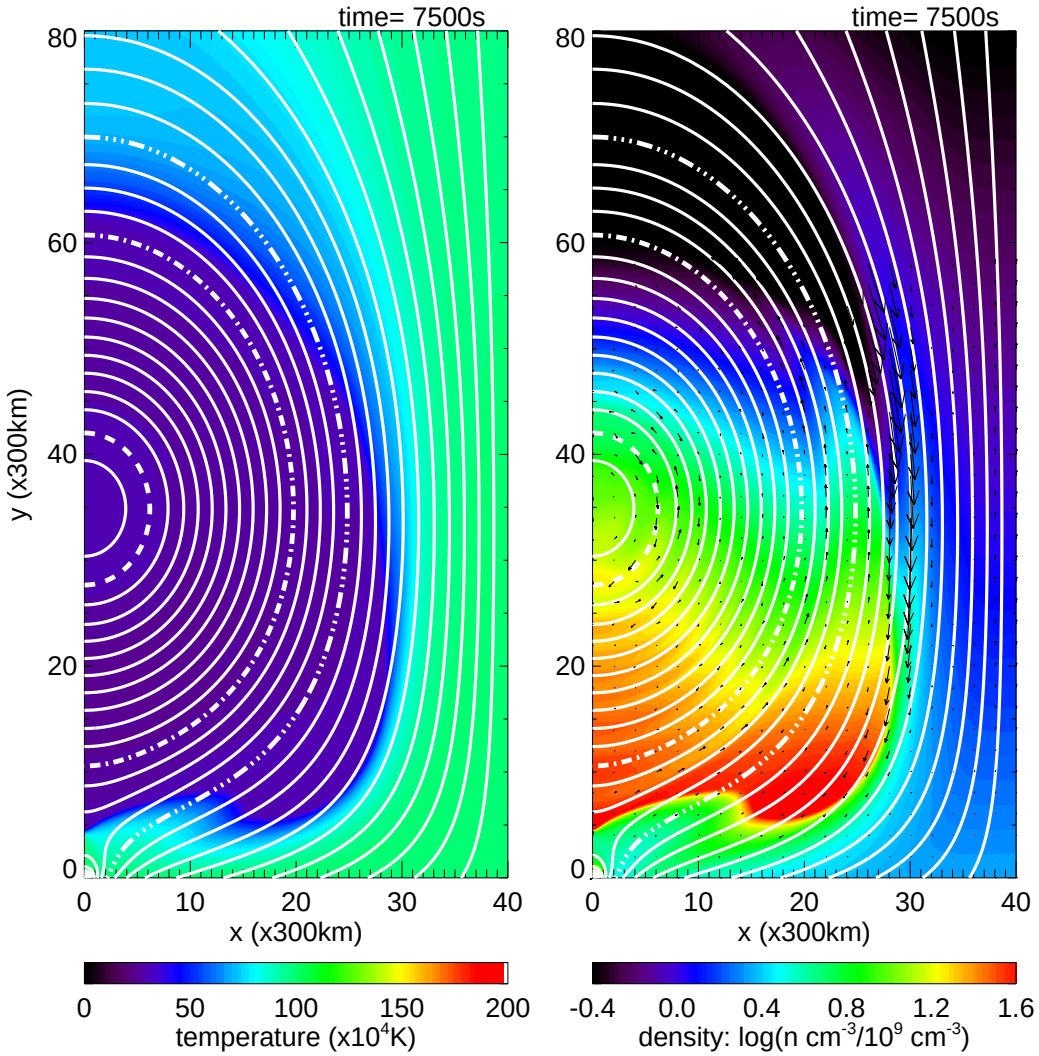

Figure 3.8: Time=7500 s.

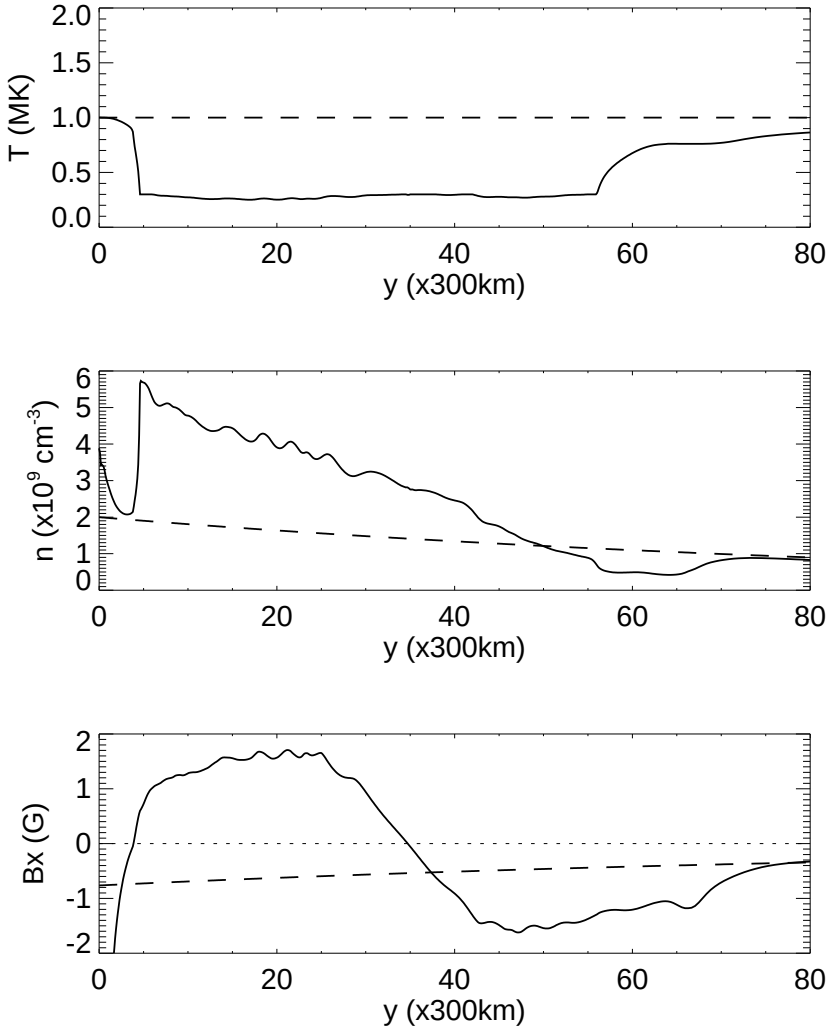

Figure 3.9: Distribution of temperature T, number density n, magnetic field component B_x along y-axis of time=5000 s in the case A. Solid lines represent the values of time=5000 s, and dashed lines represent the initial values.

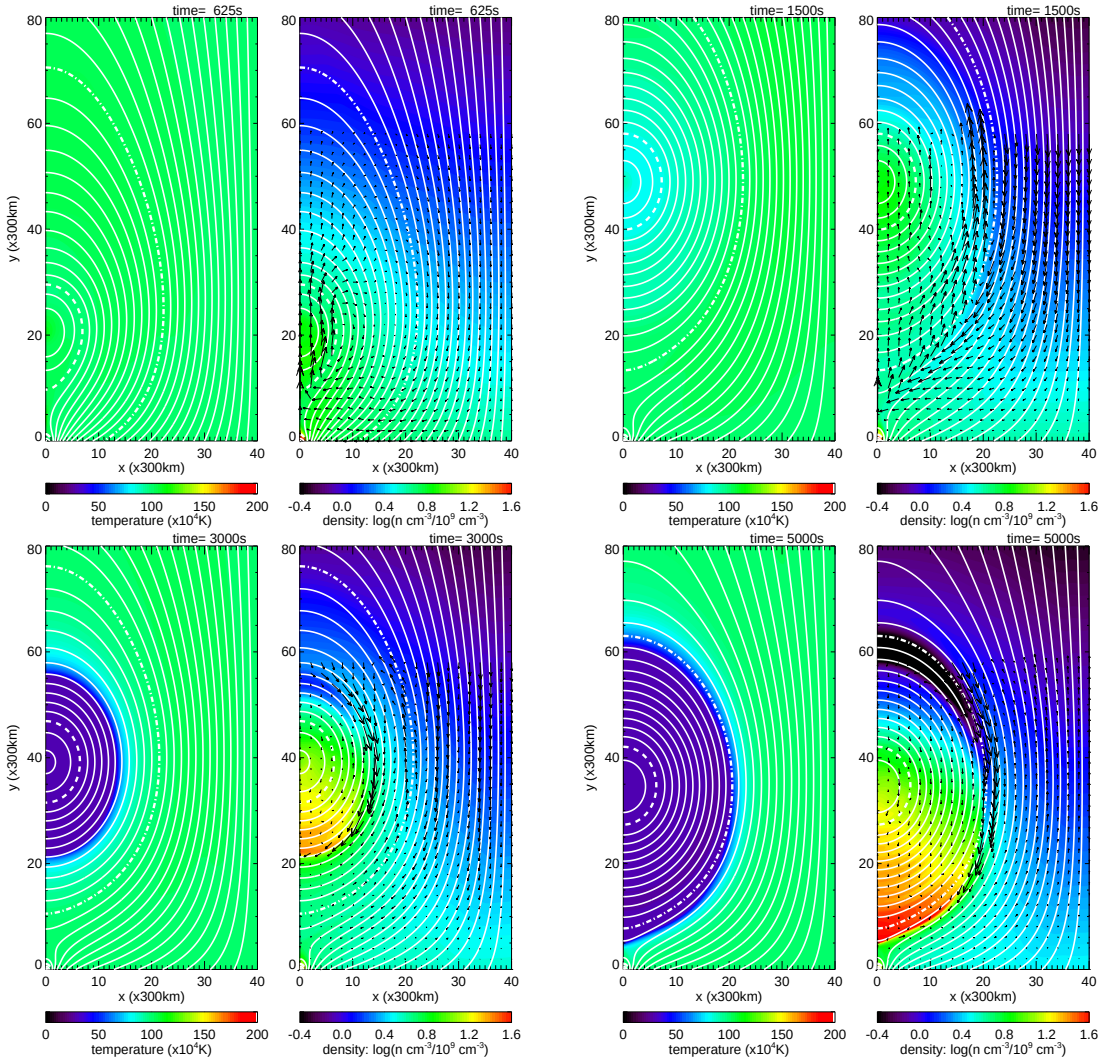

Figure 3.10: Time evolution of formation of flux rope structure and cool dense plasma layer by thermal instability. Colors represent temperature and density. White lines represent magnetic field lines, and arrows represent velocity fields.

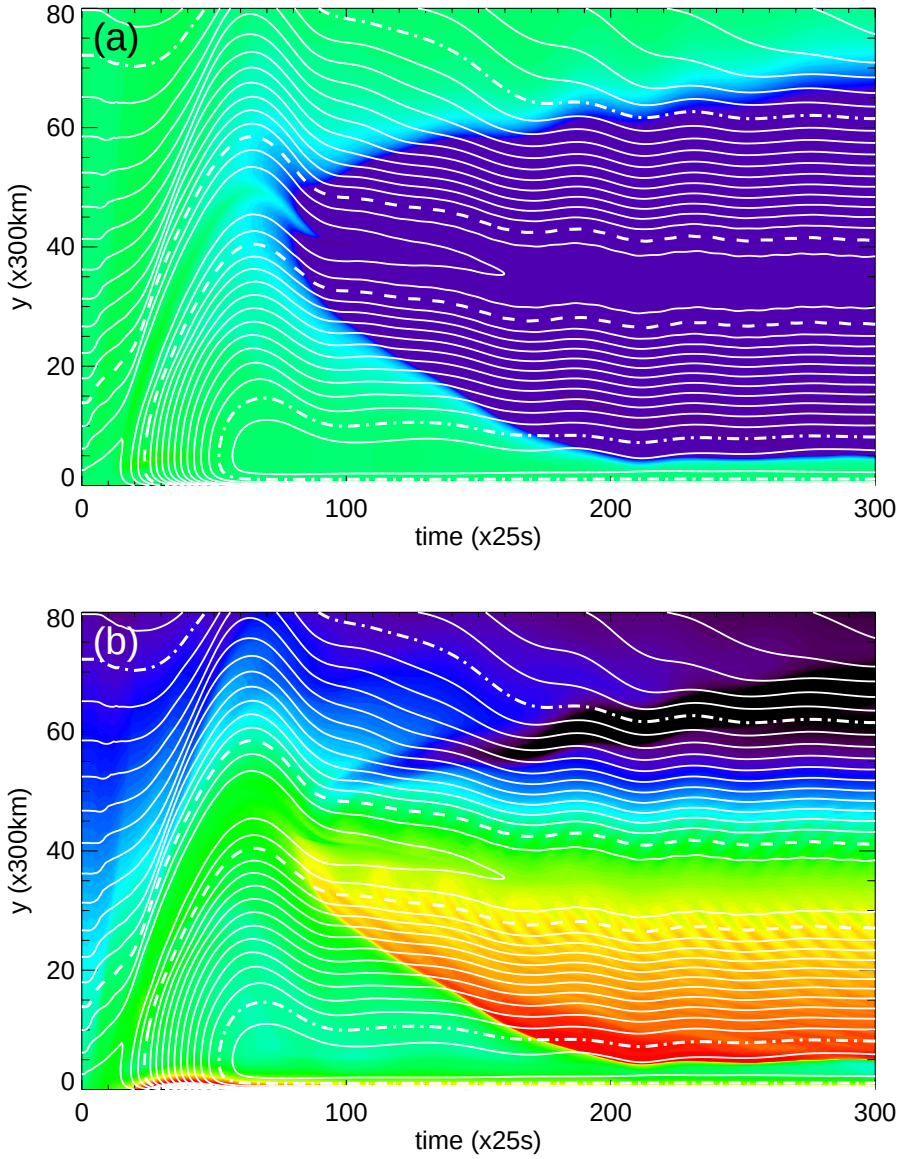

Figure 3.11: Time evolution of temperature and density along y-axis. Colors represent temperature in panel (a) and density in panel (b). Horizontal axis represents time and vertical axis represents height (y). Colors represent density, and white lines represent the positions of magnetic field.line

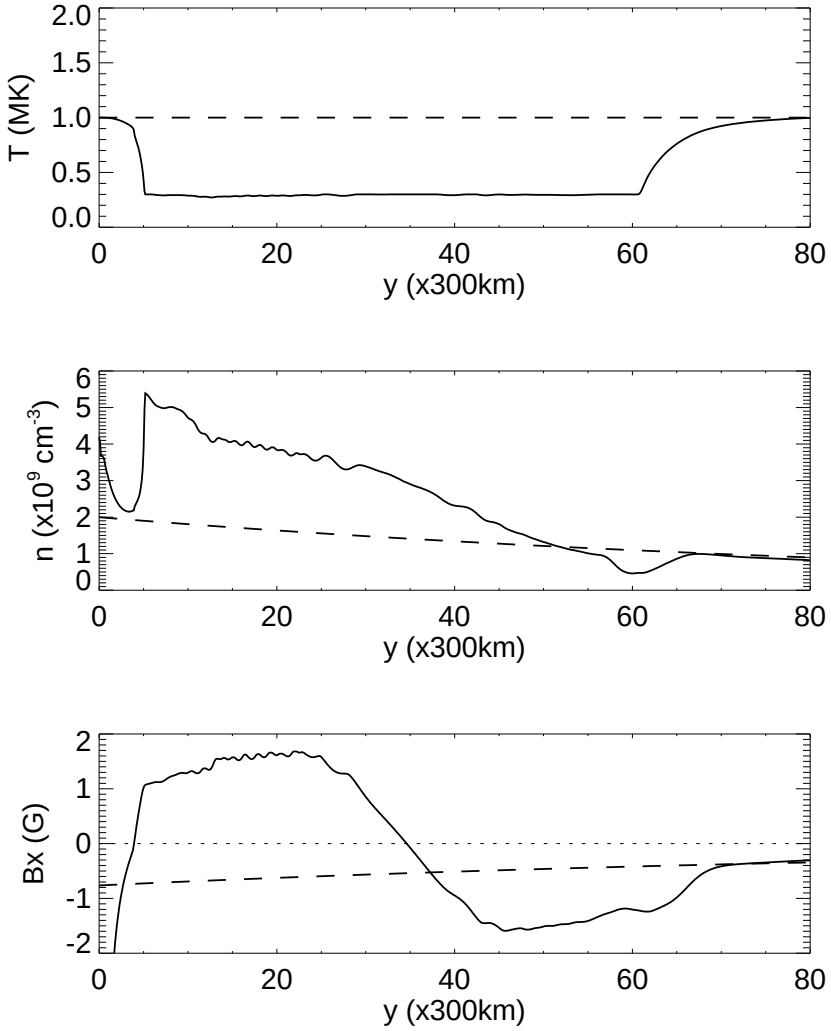

Figure 3.12: Distiribution of temperature T, number density n, magnetic field component B_x along y-axis of time=5000s in the case B. Solid lines represent the values of time=5000 s, and dashed lines represent the initial values.

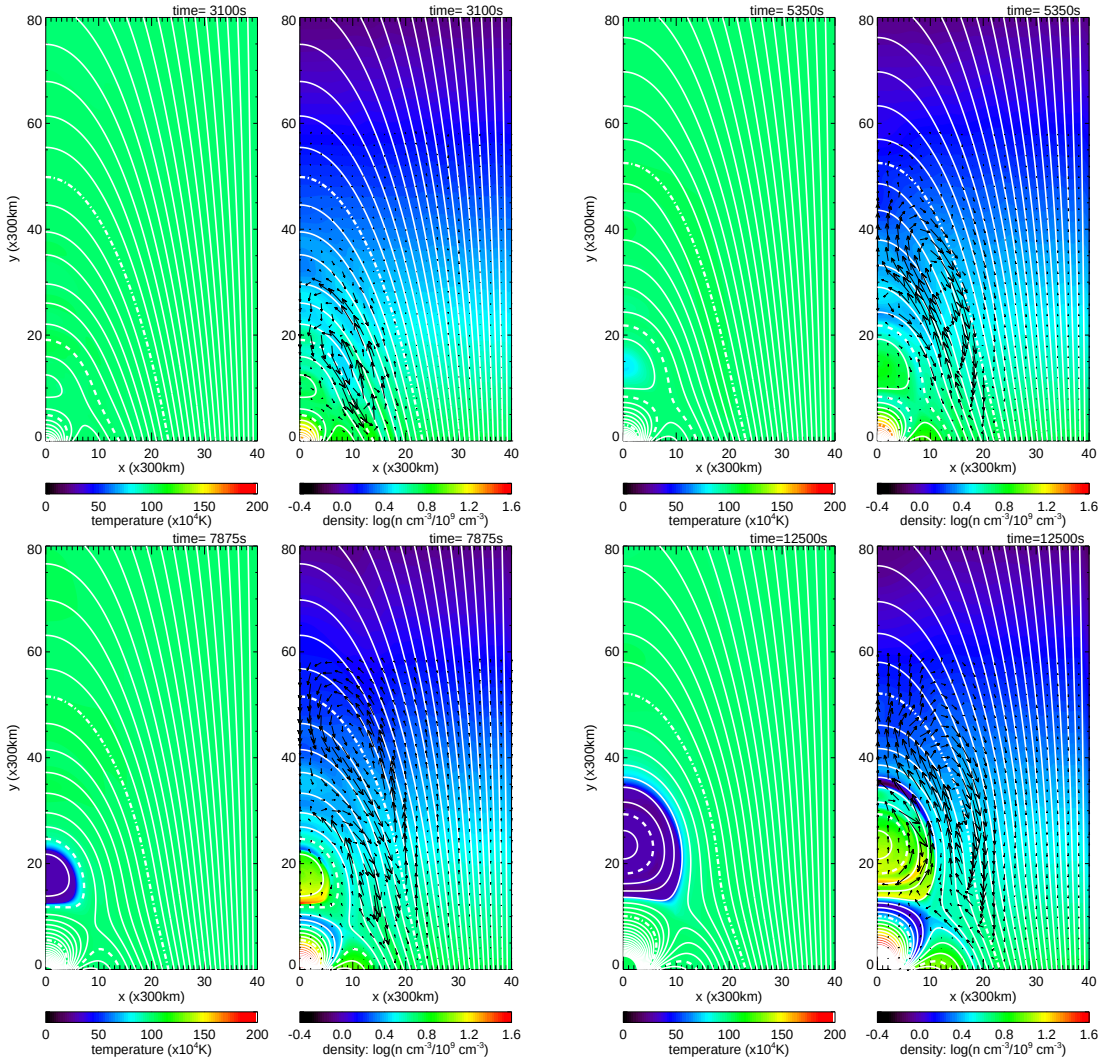

Figure 3.13: Time evolution of formation of flux rope structure and cool dense plasma layer by thermal instability. Colors represent temperature and density. White lines represent magnetic field lines, and arrows represent velocity fields.

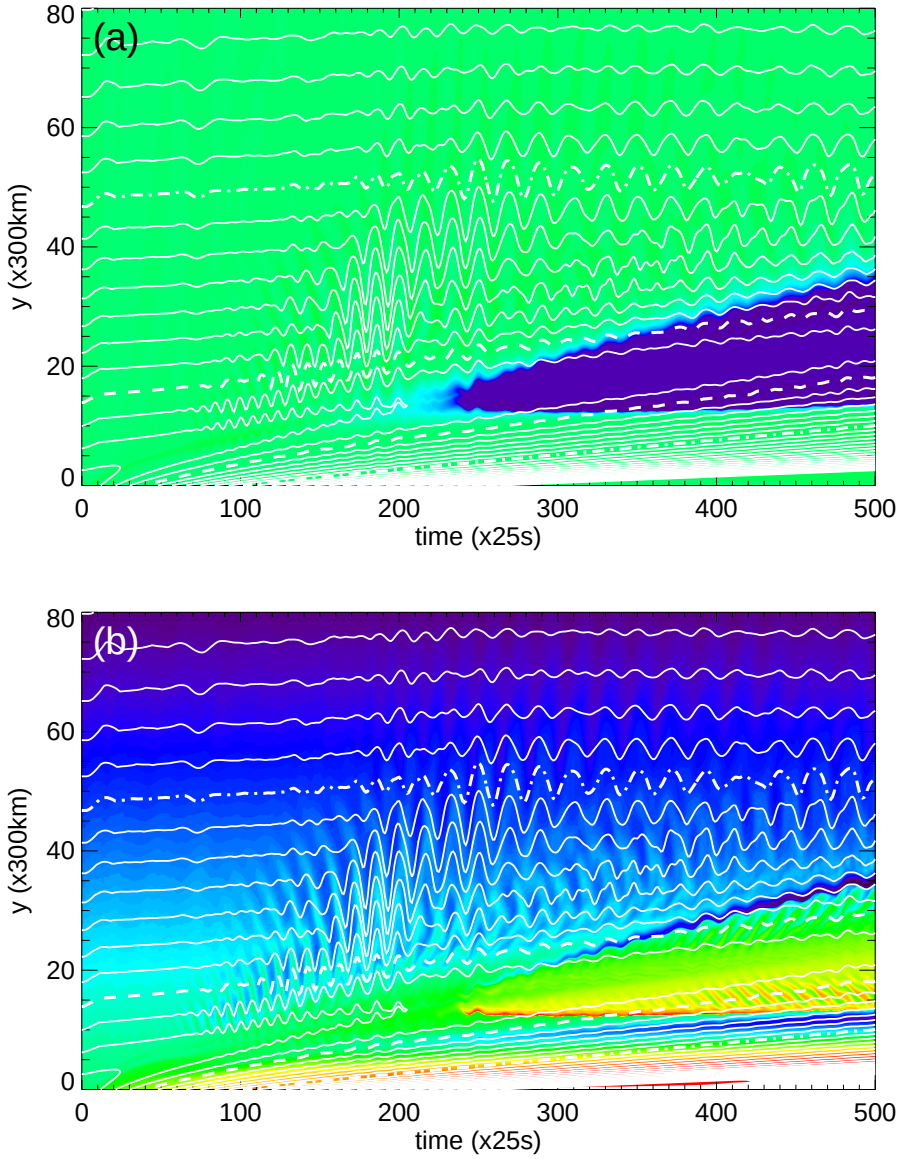

Figure 3.14: Time evolution of temperature and density along y-axis. Colors represent temperature in panel (a) and density in panel (b). Horizontal axis represents time and vertical axis represents height (y). Colors represent density, and white lines represent the positions of magnetic field.line

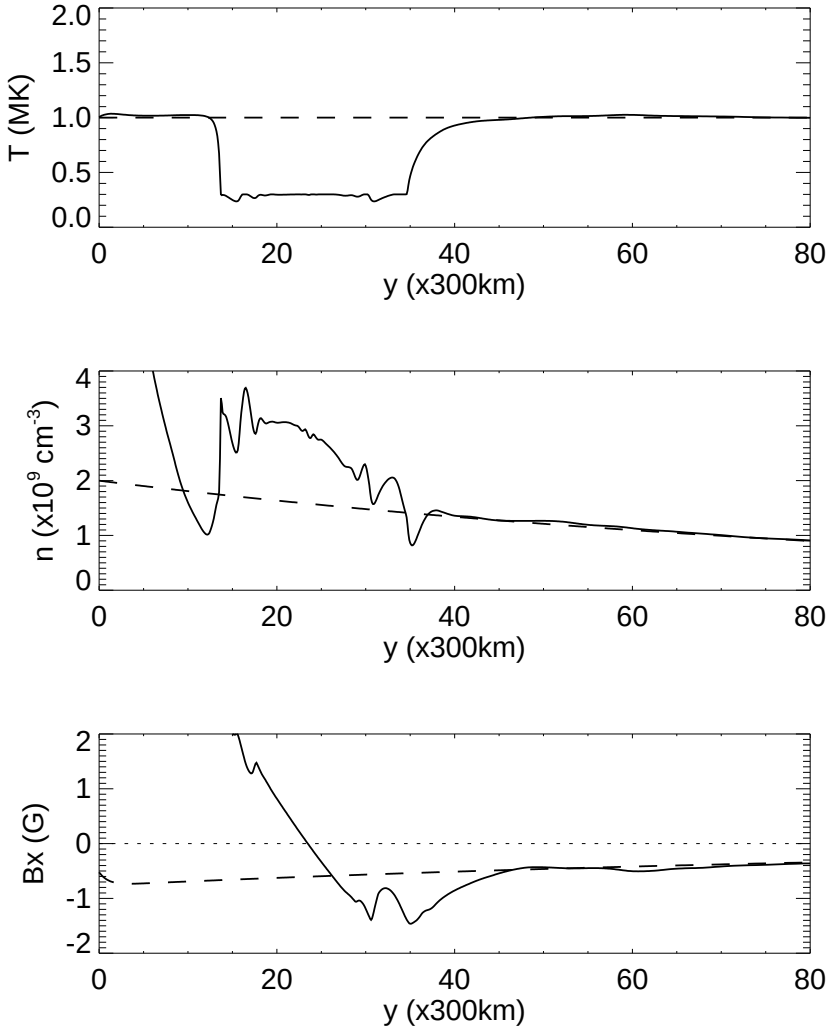

Figure 3.15: Distiribution of temperature T, number density n, magnetic field component B_x along y-axis of time=12500s in the case C. Solid lines represent the values of time=125000 s, and dashed lines represent the initial values.

3.5 DISCUSSION

3.5.1 Process for Triggering Thermal Instability

In this section, the process for triggering the thermal instability is discussed with case A as a typical example. The basic process is the same for all cases in B, C and D.

Figs. 3.16 (a) and (b) shows the temperature and the density along the short field line corresponding to the white dashed line in Fig.3.6 in case A. The horizontal axis is a distance s from the bottom of the closed line. Fig. 3.17 (a) shows the the thermal flux along the same field line in Fig.3.6. Fig. 3.17 (b) shows the radiative cooling rate and the background heating rate. Because the closed field line connects to nowhere, no thermal flux comes from the outside of the field line. At the lower part of the field line ($s < 2700$ km), the radiative cooling is larger than the background heating due to the dense plasmas trapped inside the flux rope. Because the net cooling at the lower part overwhelms the heating by the thermal flux from the upper part (Fig.3.17 (a) and (b)), the temperature at the lower part decreases. The temperature at the upper part of the field line ($s > 2700$ km) decreases subsequently to the lower part because the thermal energy is conducted (Fig. 3.17 (a)). As a result, the whole part of the field line is cooled down. This process starts from the imbalance of the radiative cooling and the background heating, hence, this is not the linear thermal instability (e.g. Field, 1965) but the radiative condensation or 'catastrophic cooling' (e.g. Antiochos & Klimchuk, 1991).

Figs. 3.18 and 3.19 are for the long closed field line (white dot-dashed line in Fig. 3.6). At the lower part of the long field line, the radiative condensation is triggered by the same process as in the short field line. The difference is net heating

at the upper part. After the radiative condensation at the lower part, the cooled plasmas stratified with the smaller scale height for the lower temperature ($T_{\rm adm}$ in our simulations) along the field line. The density at the upper part of the long field line becomes much lower than that of the short field line because the long field line has several times of the scale height (this region may be observed as the low density cavity). As a result, the radiative cooling becomes much smaller than the background heating at the upper part. Because the thermal flux conducts the energy from the upper to the lower (Fig.3.19 (a)), there is a possibility that the net heating at the upper part prevents the condensation process. In our simulations, all the closed field lines are cooled down to the temperature of $T_{\rm adm}$ eventually. If the temperature at the lower part reaches smaller value like the actual solar filaments, the net heating rate at the upper part is much larger due to the low density like in the cavities, and the thermal flux from the upper part to the lower part is much larger due to the larger gradient of temperature. Therefore, it is expected that not whole part of the long field line is cooled down in the actual corona.

Figs. 3.20 and 3.21 are for the rooted field line (white three-dotted-dashed line in Fig. 3.6). The radiative condensation is also triggered in the rooted field line adjacent to the cooled field line. As seen in Fig. 3.21 (a) and (b), the thermal flux coming from the bottom boundary compensates the net cooling and maintains the temperature of 1MK in the region from the bottom boundary to the condensation region ($0 < s < 3000$ km). Because of this hot region around the footpoint, the beginning point of density stratification ($s = 4500$ km in Fig.3.20 (b)) is higher than that of the closed field line in the flux rope. This is the reason why the discontinuity of density between the flux rope and the blob exists (see Fig.3.8).

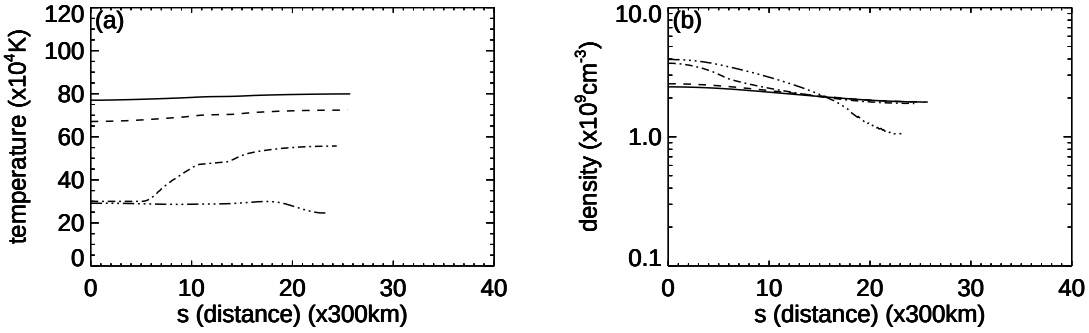

Figure 3.16: Temperature and density along the short field line. The solid line, dashed line, dot-dashed line and three-dots-dashed line represent time=2250, 2500, 2750 and 3000 s, respectively

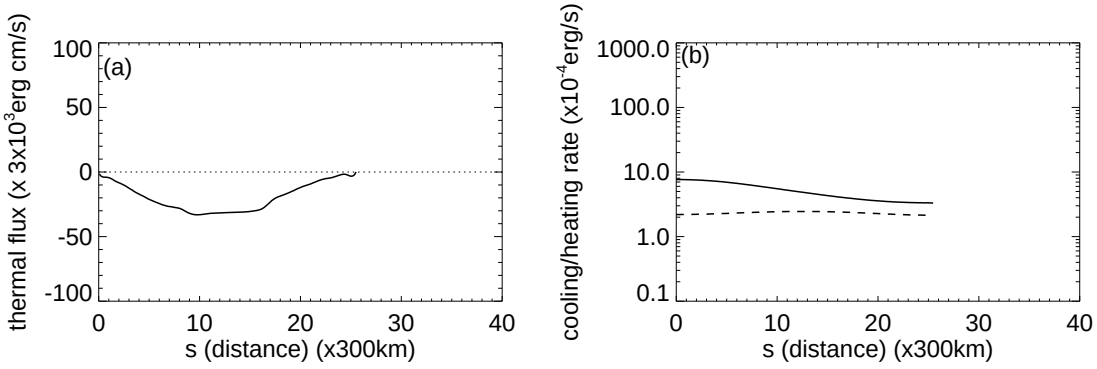

Figure 3.17: Panel (a) shows the thermal flux, and panel (b) shows the radiative cooling rate (solid line) and the background heating rate (dashed line) along the field line at time=2500 s (the dashed line in Fig.3.16).

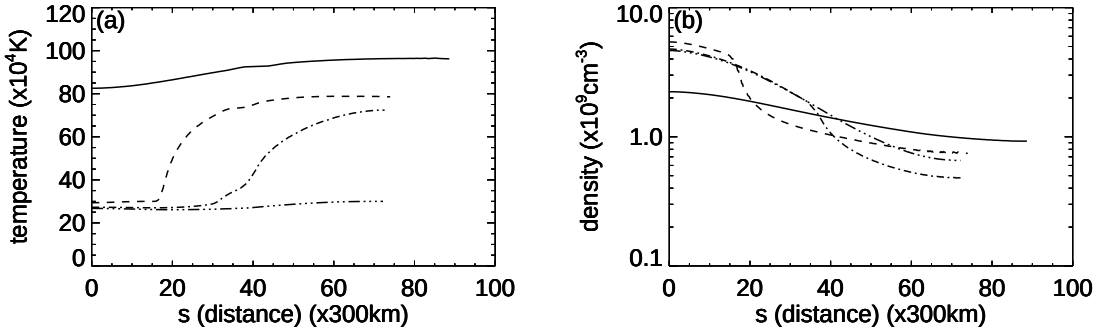

Figure 3.18: Temperature and density along the long field line. The solid line, dashed line, dot-dashed line and three-dotted-dashed line represent time=2500, 3750, 5000 and 7500 s, respectively

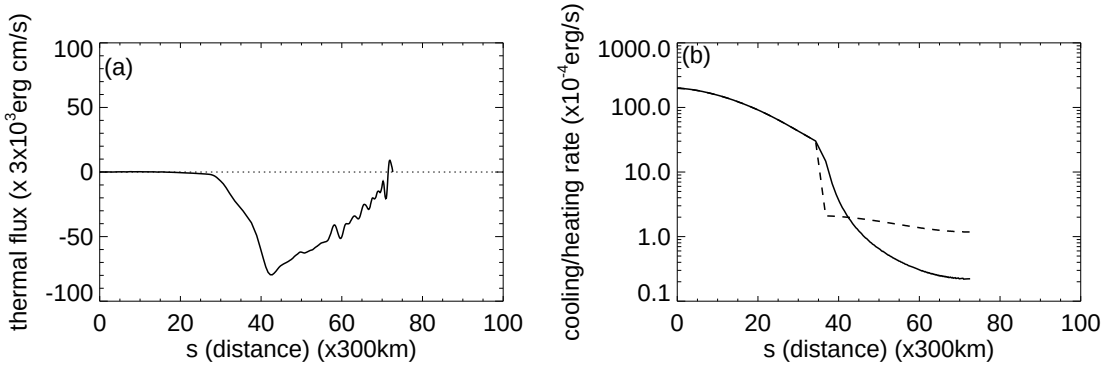

Figure 3.19: Panel (a) shows the thermal flux, and panel (b) shows the radiative cooling rate (solid line) and the background heating rate (dashed line) along the field line at time=5000 s (the dot-dashed line in Fig.3.18).

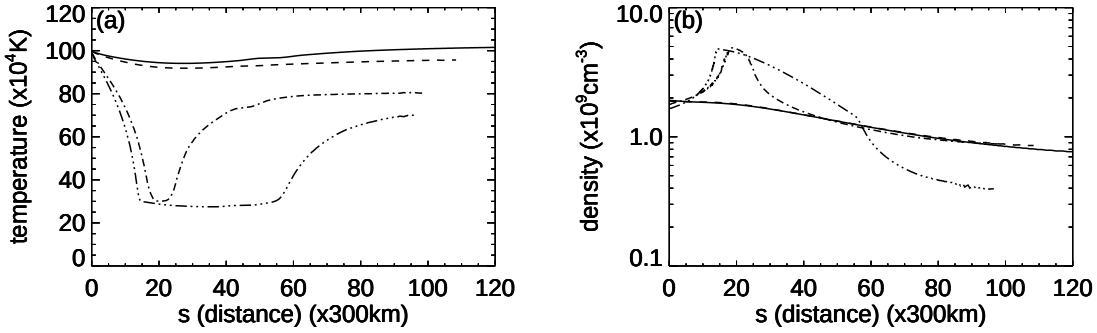

Figure 3.20: Temperature and density along the rooted field line. The solid line, dashed line, three-dots-dashed line and three-dotted-dashed line represent time=2500, 3750, 5000 and 7500 s, respectively

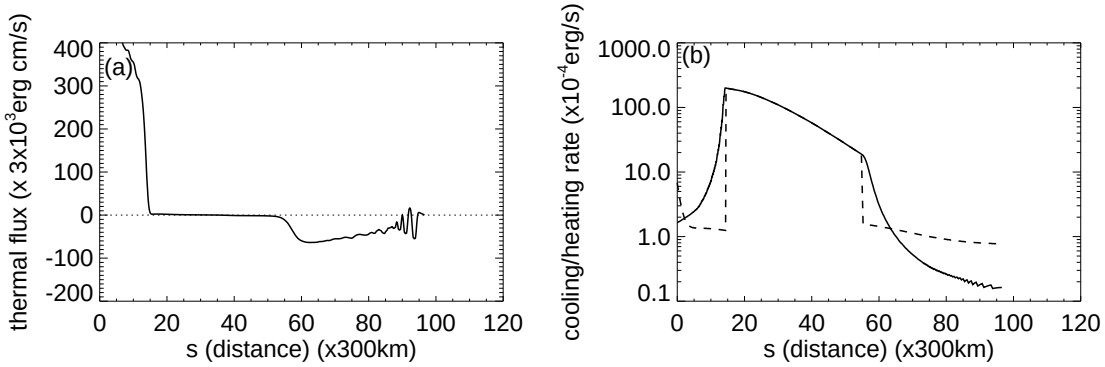

Figure 3.21: Panel (a) shows the thermal flux, and panel (b) shows the radiative cooling rate (solid line) and the background heating rate (dashed line) along the field line at time=7500 s (the three-dotted-dashed line in Fig.3.20).

3.5.2 Temperature and Density of Condensation

For the numerical reason, we apply the limitation of $T_{\rm adm}$. In this subsection, we discuss the tendency when the value of $T_{\rm adm}$ is changed. Fig.3.22 shows the maximum density in each case and $T_{\rm adm}$. The denser condensation is formed when $T_{\rm adm}$ is lower. The steeper gradient of the gas pressure by the radiative cooling forms the denser condensation. When $T_{\rm adm}$ is lower, the radiative cooling reaches larger value and the steeper pressure gradient is caused. This is the reason that the denser condensation is formed when the temperature is lower. In our simulations, the temperature of the condensation is too high to explain that of the real solar filament (0.01 - 0.1MK). Without the limitation of Eq.3.12, the temperature of the condensation is expected to be lower, and the denser condensation must appear. We estimate the number density of the filament of $T = 0.01$MK by the least square fitting of the maximum density. The fitting function is

$$n = \zeta \frac{1}{T} + \epsilon, \tag{3.38}$$

where ζ and ϵ are the fitting parameters. A set of 6 data in each converging type and emerging flux type are fitted (Table.3.2 and solid lines in Fig.3.22). Because ϵ is small enough to neglect, we obtain the scaling formula as

$$nT = \zeta. \tag{3.39}$$

This formula is physically justified as follows. The dense plasmas accumulate along the field lines. From the conservation of mass along the magnetic field line in a

length of the scale hight ,

$$M(\chi) = n_{\rm cor}\chi H_{\rm cor} = n\frac{k_B T}{m g_{\rm cor}} \tag{3.40}$$

where $H_{\rm cor} = k_B T_{\rm cor}/m g_{\rm cor}$ is the scale hight of the coronal temperature, χ is the length of the closed field line with the unit of $H_{\rm cor}$ and $M = (\chi k_B/m g_{\rm cor})\zeta$ is total mass along the closed field line. The values of ζ is consistent with mass along the closed field line in our simulations, and ζ is larger in converging type because the length of the closed field line is longer, and ζ is smaller in emerging flux type in which the closed field line is shorter. We estimate $n_{0.01\rm MK}$, the number density of the filament of 0.01MK, by this formula (Table. 3.2), and $n_{0.01\rm MK}$ is 85 times larger than the coronal density in the converging type and 58 times in the emerging flux type, where coronal density is 2×10^9 cm^{-3} in our simulations. It is concluded that our model has a possibility to reproduce the density of filaments, which is 10 - 100 times larger than that of the surrounding corona.

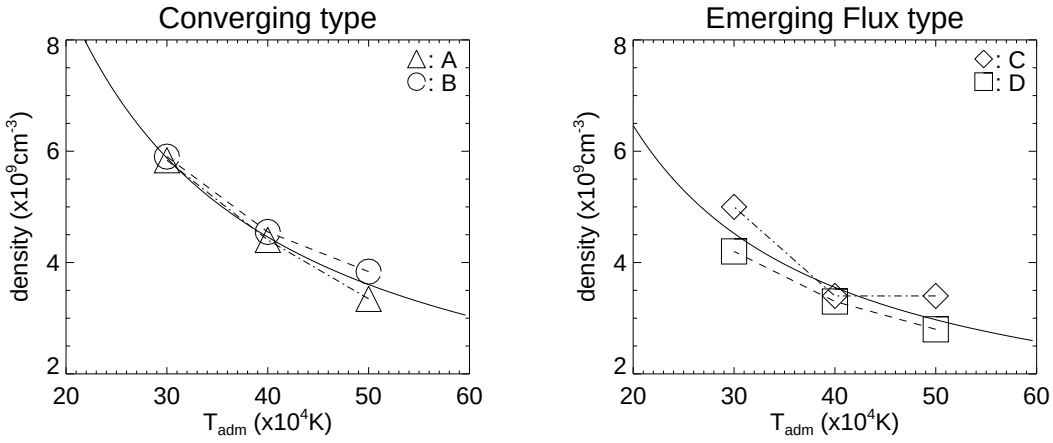

Figure 3.22: Maximum density in each case and $T_{\rm adm}$. The triangles, circles, diamonds, and squares represent the case A, B, C, and D, respectively. Solid lines are the fitted line.

	converging	emerging flux
ζ ($\times 10^{15}$ cm^{-3} K)	1.70	1.16
ϵ ($\times 10^{9}$ cm^{-3})	0.19	0.64
$n_{0.01\mathrm{MK}}$ ($\times 10^{9}$ cm^{-3})	170	116

Table 3.2: Results of fitting parameters and estimated number density of the filament of 1MK

3.5.3 Limitation of 2.5-dimensional simulations and prospect of three-dimensional simulations

Due to 2.5-dimensional simulation, the z-directional gradient is not concerned in our simulations. The filaments in our simulation correspond to long filaments, and the heat flux from the two footpoints by which filaments connect to the chromosphere is neglected. If filaments have a moderate length like active region filaments, the length of the flux rope must be one of the critical condition for triggering the thermal instability. The criteria would be almost the same as those reported by previous one-dimensional simulations ($>$ 80Mm, Karpen et al., 2003) or shorter due to the rotation of field lines inside the flux rope. In 2.5-dimensional simulation, the concave-up structure (dip) of the flux rope can not be reproduced (see Fig.3.23). The dip is suitable for accumulating mass, and the denser filament would be reproduced by coupling with the stronger radiative cooling.

The three-dimensional structure also affects the mechanical stability of the filament system. In two-dimensional case, the flux rope quickly descends. In our simulation, the flux rope stops to descend by the bottom boundary condition. On the other hand, if concave-up structure is formed in three-dimensional simulations (Fig.3.23), the upward magnetic tension force will help to sustain the condensation. The magnetic field strength and the initial density also affect the mechanical

balance. In the emerging flux type like case C and D in this study, the flux rope does not drop into the chromosphere because the emerging flux helps to sustain the flux rope. For the discussion of the mechanical balance, we have to investigate

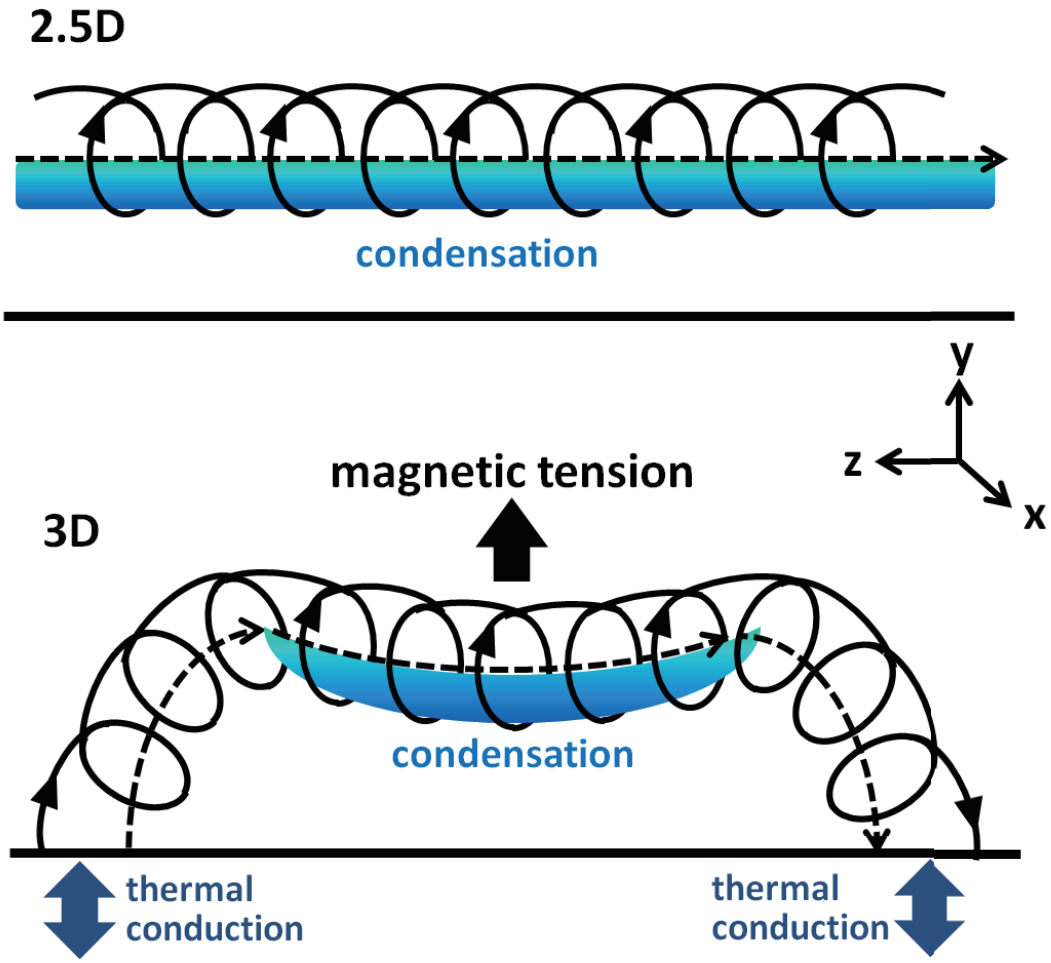

Figure 3.23: Schematic drawings of 2.5-dimensional and three-dimensional flux rope

3.6 SUMMARY

In this chapter, we investigate the formation mechanism of solar filaments by 2.5-dimensional MHD simulations. We succeeded in reproducing the filaments of the KR model with condensation process by the levitation-condensation model.

We tested two types of the heating term and two mechanisms for forming the flux rope. The process to trigger the thermal instability is common for all cases A -D. The thermal imbalance between the radiative cooling and the background heating by the levitated dense plasmas in the closed field line trigger the thermal instability, leading to the formation of condensation.

For the more detailed discussion of the triggering mechanism for thermal instability, three-dimensional simulations are necessary. It is expected that the length of the flux rope is one of the critical condition for thermal instability and that the mechanical balance of the filament's system also can be discussed in three-dimensional case.

Chapter 4

Conclusion

We investigate the mechanisms for formation and eruption of filaments by two-dimensional MHD simulations. At first, The mechanisms of eruptions associated with interaction between newly emerging flux and coronal arcade fields were investigated by 2.5-dimensional MHD simulations. We found that two possible eruptive mechanisms exist, and determined their degree of dependence on the parameters of magnetic scale height of the arcade field, the amount of flux, and the location of emerging flux. The CA-type mechanism is dominant when the location of emerging flux surrounds the edges of arcades. This type shows a linear tendency which can be represented as formula (2.47), namely, the formation and eruption of a plasmoid occurs when the location of emerging flux is close to the arcade field and the amount of flux introduced into the corona is large enough. The eruptions are also likely to occur when the magnetic scale height is large (this is the same situation as when the arcade is strongly sheared). The RC-type mechanism is dominant when emerging flux surrounds the PIL. The parameter dependence shows that eruptions are likely to occur when a small amount of magnetic flux is introduced and when the arcade is strongly sheared. The results of our parameter survey are qualitatively consis-

tent with previous observational studies (Feynman & Martin 1995, Xu et al. 2008) and agree quantitatively with the observed physical values of miniature filament eruptions. We conclude that our model has the potential to predict eruptions when the shear angle of the arcade field, the ratio of magnetic flux, and the location of emerging flux relative to the arcade field are observed.

Next, the formation mechanism of the Kuperus-Raadu type filaments was investigated by 2.5-dimensional MHD simulations including thermal conduction, radiative cooling and gravity. We proposed levitation-condensation model, in which the relatively dense plasmas levitated by the flux rope are condensed by the thermal instability, and demonstrated it by 2.5-dimensional MHD simulations. We tested two types of the heating term and two mechanisms for forming the flux rope and succeeded in reproducing the filament of the KR model in every case. The process to trigger the thermal instability is common for all cases. The thermal imbalance between the radiative cooling and the background heating by the levitated dense plasmas in the closed field line triggers the thermal instability, leading to the formation of cool dense condensation. The background heating only affects the duration of gradual decreasing in temperature before the thermal instability. We obtained the scaling formula about the temperature and density. We conclude the model has a potential to explain the actual filaments' density, which is 10 - 100 times larger than that of surrounding corona. For the more detailed discussion of the triggering mechanism for thermal instability, three-dimensional simulations are necessary. It is expected that the length of the flux rope is one of the critical condition for thermal instability and that the mechanical balance of the filament's system also can be discussed in three-dimensional case.

Acknowledgements

I would like to express my deepest gratitude to Associate Professor Yokoyama, Takaaki, my supervisor, for his innumerably insightful comments and continuous encouragement throughout the course of my study. I would like to thank our laboratory members, Kitagawa, N., Toriumi, S., Hotta, H., Matsui, Y., Iijima, H., Wang, S., Kono, S., and Nasuda, T. for helpful discussions and daily seminars. I would also express my great thanks to Dr. Iida, Y., and Dr. Antolin, P. for valuable discussions and suggestions. Discussions with members of the Solar-Terrestrial Physics Colloquium, the Space and Planetary Science Group have been also illuminating. Finally, I would like to thank my family for their continuous support.

Numerical computations were carried out on Cray XC30 and the general-purpose PC farm at Center for Computational Astrophysics, National Astronomical Observatory of Japan.

References

Antiochos, S. K., & Klimchuk, J. A. 1991, ApJ, 378, 372

Antiochos, S. K., MacNeice, P. J., Spicer, D. S., & Klimchuk, J. A. 1999, ApJ, 512, 985

Berger, T. E., Liu, W., & Low, B. C. 2012, ApJ, 758, L37

BĄk-Stęślicka, U., Gibson, S. E., Fan, Y., et al. 2013, ApJ, 770, L28

Bobra, M. G., van Ballegooijen, A. A., & DeLuca, E. E. 2008, ApJ, 672, 1209

Carmichael, H. 1964, NASA Special Publication, 50, 451

Chen, P. F. 2011, Living Reviews in Solar Physics, 8, 1

Chen, P. F., & Shibata, K. 2000, ApJ, 545, 524

Fan, Y., & Gibson, S. E. 2007, ApJ, 668, 1232

Feynman, J., & Martin, S. F. 1995, J. Geophys. Res., 100, 3355

Field, G. B. 1965, ApJ, 142, 531

Gopalswamy, N., Lara, A., Yashiro, S., Nunes, S., & Howard, R. A. 2003, in ESA Special Publication, Vol. 535, Solar Variability as an Input to the Earth's Environment, ed. A. Wilson, 403–414

Hirayama, T. 1974, Sol. Phys., 34, 323

Isobe, H., Miyagoshi, T., Shibata, K., & Yokoyama, T. 2006, PASJ, 58, 423

Jing, J., Yurchyshyn, V. B., Yang, G., Xu, Y., & Wang, H. 2004, ApJ, 614, 1054

Karpen, J. T., & Antiochos, S. K. 2008, ApJ, 676, 658

Karpen, J. T., Antiochos, S. K., Hohensee, M., Klimchuk, J. A., & MacNeice, P. J. 2001, ApJ, 553, L85

Karpen, J. T., Antiochos, S. K., Klimchuk, J. A., & MacNeice, P. J. 2003, ApJ, 593, 1187

Karpen, J. T., Tanner, S. E. M., Antiochos, S. K., & DeVore, C. R. 2005, ApJ, 635, 1319

Kippenhahn, R., & Schlüter, A. 1957, ZAp, 43, 36

Kliem, B., Titov, V. S., & Török, T. 2004, A&A, 413, L23

Kliem, B., & Török, T. 2006, Physical Review Letters, 96, 255002

Kopp, R. A., & Pneuman, G. W. 1976, Sol. Phys., 50, 85

Koyama, H., & Inutsuka, S.-i. 2004, ApJ, 602, L25

Kudoh, T., Shibata, K., & Matsumoto, R. 1999, in Astrophysics and Space Science Library, Vol. 240, Numerical Astrophysics, ed. S. M. Miyama, K. Tomisaka, & T. Hanawa, 203

Kuperus, M., & Raadu, M. A. 1974, A&A, 31, 189

Kusano, K., Bamba, Y., Yamamoto, T. T., et al. 2012, ApJ, 760, 31

Kusano, K., Maeshiro, T., Yokoyama, T., & Sakurai, T. 2004, ApJ, 610, 537

Labrosse, N., Heinzel, P., Vial, J.-C., et al. 2010, Space Sci. Rev., 151, 243

Leroy, J. L., Bommier, V., & Sahal-Brechot, S. 1984, A&A, 131, 33

Liu, K., Wang, Y., Shen, C., & Wang, S. 2012, ApJ, 744, 168

Low, B. C., & Hundhausen, J. R. 1995, ApJ, 443, 818

Luna, M., Karpen, J. T., & DeVore, C. R. 2012, ApJ, 746, 30

Mackay, D. H., Karpen, J. T., Ballester, J. L., Schmieder, B., & Aulanier, G. 2010, Space Sci. Rev., 151, 333

Magara, T. 2001, ApJ, 549, 608

—. 2004, ApJ, 605, 480

Martens, P. C., & Zwaan, C. 2001, ApJ, 558, 872

Notoya, S. 2006, The University of Tokyo,Master thesis

Petschek, H. E. 1964, NASA Special Publication, 50, 425

Pevtsov, A. A., Panasenco, O., & Martin, S. F. 2012, Sol. Phys., 277, 185

Ren, D. B., Jiang, Y. C., Yang, J. Y., et al. 2008, Ap&SS, 318, 141

Rosner, R., Tucker, W. H., & Vaiana, G. S. 1978, ApJ, 220, 643

Sakajiri, T., Brooks, D. H., Yamamoto, T., et al. 2004, ApJ, 616, 578

Spitzer, L. 1962, Physics of Fully Ionized Gases

Sturrock, P. A. 1966, Nature, 211, 695

Török, T., & Kliem, B. 2005, ApJ, 630, L97

Tsuneta, S., Hara, H., Shimizu, T., et al. 1992, PASJ, 44, L63

van Ballegooijen, A. A., & Martens, P. C. H. 1989, ApJ, 343, 971

Wang, J., Li, W., Denker, C., et al. 2000, ApJ, 530, 1071

Wang, Y.-M., & Sheeley, Jr., N. R. 1999, ApJ, 510, L157

Xia, C., Chen, P. F., & Keppens, R. 2012, ApJ, 748, L26

Xiao, F., Yabe, T., Nizam, G., & Ito, T. 1996, Computer Physics Communications, 94, 103

Xu, X.-Y., Fang, C., & Chen, P.-F. 2008, Chinese Astron. Astrophys., 32, 56

Yokoyama, T., & Shibata, K. 1994, ApJ, 436, L197